Geochimica et Cosmochimica Acta 369 (2024) 93–110

Contents lists available at ScienceDirect

Geochimica et Cosmochimica Acta

journal homepage: www.elsevier.com/locate/gca

Ce and Eu anomalies in zircon as indicators of oxygen fugacity in subsolidus systems

Dustin Trail [a,*], Wriju Chowdhury [a,b], Nicholas D. Tailby [c], Michael R. Ackerson [b]

[a] Department of Earth & Environmental Sciences, University of Rochester, Rochester, NY 14627, USA
[b] Department of Mineral Sciences, Smithsonian Institution, Washington, DC, USA
[c] Division of Earth Science, School of Environmental and Rural Science, University of New England, Armidale, NSW, Australia

ARTICLE INFO

Associate editor: Bernard Charlier

Keywords:
Zircon
Oxygen fugacity
Ce anomaly
Eu anomaly
Critical minerals
Hydrothermal fluids

ABSTRACT

Quantifying the oxygen fugacity (fo_2) of high temperature lithospheric fluids, including hydrothermal systems, presents a challenge because these fluids are difficult to capture and measure in the same manner as quenched glasses of silicate melts. The chemical properties of fluids can however be inferred through mineral proxies that interacted with the fluids through precipitation or recrystallization. Here, we present hydrothermal experiments to quantify the partition coefficients of rare earth elements (REEs) – including redox-sensitive Ce and Eu – between zircon and fluid. Experiments were conducted in a piston cylinder device at temperatures that range from 1200 to 800 °C under fo_2-buffered conditions in a SiO_2-ZrO_2-NaCl-REE-oxide system, and similar experiments were performed in the absence of NaCl (31 total experiments). The fo_2 was buffered to values that range from approximately 3 log units below to 7 log units above the fayalite magnetite quartz equilibrium. Zircon REE concentrations were quantified using laser ablation inductively coupled plasma mass spectrometry whereas the quenched fluids were extracted and measured by solution-based inductively coupled plasma mass spectrometry. Zircon Ce anomalies, quantified relative to La and Pr, exhibit sensitivity to oxygen fugacity and temperature and our preferred calibration is:

$$log\left[\left(\frac{Ce}{Ce^*}\right)_D - 1\right] = (0.237 \pm 0.040) \times log(fo_2) + \frac{9437 \pm 640}{T(K)} - 5.02 \pm 0.38$$

where the Ce anomalies are calculated from the partition coefficients for La, Ce, and Pr. Zircon Eu anomalies are also a function of oxygen fugacity though they exhibit no systematic dependence on T. Our preferred calibration is described by:

$$\left(\frac{Eu}{Eu^*}\right)_D = \frac{1}{1+10^{0.30\pm0.04-\lvert 0.27\pm0.03\rvert \times \Delta FMQ}}$$

We performed additional calculations, in which lattice strain parabolas were fit to all non-redox sensitive rare earth elements that were added to the starting composition (i.e., La, Pr, Sm, Gd, Dy, Ho, Tm, Lu) as an alternate means to calculate anomalies. This method yields broadly similar results, though we prefer the La-Pr calibrations due to the non-systematic REE patterns frequently encountered with hydrothermal zircons; e.g., LREE zircon enrichment relative to other REEs. These experiments are applied to quantify the fo_2 of fluids during mineralization of critical element-bearing systems, and separately to calculate the oxygen fugacity values of fluids formed during plate boundary processes.

1. Introduction

The thermodynamic variable oxygen fugacity (fo_2) can take on substantially different values among different regions and reservoirs of the Earth. The most distinct example of this is the oxidation state of our present-day atmosphere whose fo_2 is 0.21, which is out of equilibrium and significantly more oxidized than fluids or melts derived from the interior of our planet. For instance, the fo_2 recorded in mineral oxybarometers of the Bishop Tuff (BT) magma was $\sim 10^{-14}$ at 800 °C when the magma entered the uppermost portion of the continental crust before eruption *ca.* 760 ka (Hildreth and Wilson, 2007; *cf.* Ghiorso and Gualda, 2013). As another example, the fo_2 of hydrothermal (HT) fluids derived from circulating seawater that interacted with the oceanic crust was calculated to be $\sim 10^{-29}$ at 400 °C, where imminent mixing with the

* Corresponding author.
E-mail address: dtrail@ur.rochester.edu (D. Trail).

https://doi.org/10.1016/j.gca.2024.01.024
Received 29 July 2023; Accepted 23 January 2024
Available online 7 February 2024

comparatively oxidized seawater would yield a relatively more oxidized product (McCollom and Shock, 1998). While these absolute values demonstrate the significant difference between oxidation state of different reservoirs, it is often more convenient to consider the oxygen fugacity of a system relative to some well-known oxidation–reduction reaction. If the oxygen fugacity is expressed relative to a well-known reaction such as the fayalite magnetite quartz (FMQ) equilibrium, there is no explicit need to specify the temperature of the system. By employing the FMQ redox reference buffer as a point of reference, we can convey fo_2 of a system by indicating its proximity to the buffer in log units (positive or negative). For example, FMQ+1 is one $\log_{10}$ unit more oxidized than the FMQ buffer at a given temperature. For the BT and HT systems above, the oxygen fugacity can be expressed as FMQ+0.8 and FMQ-0.3, respectively, where the BT magma on this relative scale is more oxidized than the HT fluid. The widespread application of the Δ-notation is also made possible by virtue of the different known mineral buffer reactions being broadly parallel in 1/T-log(fo_2) space.

This notation can be particularly useful when different systems come in contact and chemically interact, which often initiates when physical transport of material in the liquid state – e.g., silicate melts and aqueous fluids – impinge upon another system with distinct physicochemical characteristics (e.g., dykes, volcanic eruptions, hydrothermal fluid circulation). For silicate melts, tracking fo_2 has reshaped our understanding of Earth's chemistry. For instance, research has led to a better understanding of how C-N-O-S-H volatiles in igneous systems affect the chemical composition and development of the atmosphere (Delano, 2001; Trail et al., 2011a; Hirschmann, 2012; Sossi et al., 2020). Studies have also examined the mantle oxidation state change over time (Canil, 2002; Berry et al., 2008; Gao et al., 2022), the complex redox interactions that occur in subduction zones (Kelly and Cottrell, 2009; Bucholz and Kelemen, 2019; Holycross and Cottrell, 2023), and the availability of critical mineral resources (Candela, 1992; Blevin and Chappell, 2011; Yardley and Bodnar, 2014). The importance of system oxidation state has also led to substantial effort to map the valence state of transition metals such as Fe, V, and Cr in experimental and natural silicate quenched liquids (glasses), to the intensive variable oxygen fugacity (Carmichael, 1991; Holycross and Cottrell, 2022). In many of these cases, analysis of the glass is the most direct means for revealing information about the oxidation state of the system (Berry et al., 2008; Cottrell and Kelly, 2011; Cottrell et al., 2021), which is capable of quenching in and preserving valence states that reflect molten conditions at least for S and Fe (Muth and Cottrell, 2023). Mineral chemistry may also be utilized as a proxy for fo_2 when the systems are not directly accessible/poorly preserved, or to explore how fo_2 changes with time by examining redox-sensitive chemical variations in minerals (Ghiorso and Evans, 2008; Trail et al., 2015; Tailby et al., 2023).

High T lithospheric fluids represent one reservoir which is difficult to access directly for measurements, and they are also poorly preserved. Even so, the properties of these fluids are crucial to characterize because they influence mineral formation, chemical potentials during metamorphism, and volatile/ion transport in the lithosphere. For instance, high temperature fluids may take part in high-P metamorphic reactions (>5 kbar), or they may be generated directly as a result of metamorphic dehydration reactions (Hacker et al., 2003; Baxter and Caddick, 2013). At shallower depths, magmatic differentiation may result in generation of hydrothermal fluids that interact and mix with near surface fluids (Rancourt et al., 2001; Colman et al., 2019). Fluid inclusion studies can provide compositional constraints such as salinity of high temperature fluids (Aranovich et al., 2014; Yardley and Bodnar, 2014), which we complement here by targeting the fo_2 of lithospheric fluids with mineral chemistry as a proxy.

Here we expand on our earlier work to explore the potential of zircon chemistry to quantify the oxidation state of subsolidus systems (Trail and McCollom, 2023). Zircon chemistry has been shown to provide a chemical record of a variety of high T non-igneous conditions (e.g., Hoskin and Black, 2000; Hoskin, 2005; Rubatto et al., 2011; Rubatto, 2017; Walsh and Spandler, 2023). Moreover, zircon chemical information can be contextualized with absolute age information via the U-Pb geochronology system (Schmitt, 2011; Schoene, 2014) and crystallization temperature (Ferry and Watson, 2007). We present zircon-fluid partitioning experiments to constrain the compatibility of rare earth element (REE) the zircon vs. fo_2 and temperature. We focus on Ce and Eu, where in terrestrial systems they are found in the redox states of Ce^{4+}/Ce^{3+} and Eu^{3+}/Eu^{2+}. We also report on the compatibility of other REEs in the zircon structure that do not exhibit sensitivity to oxygen fugacity. Together, these partition coefficients are used to calibrate the compatibility of Ce and Eu relative to other non-redox sensitive REEs in zircon.

2. Methods

2.1. Background

The partition coefficient of a rare earth element in zircon is defined as the concentration of a specific element divided by the concentration of the same element in the coexisting fluid ($D_{REE}^{zrc/fluid}$). In a high temperature terrestrial fluid, Ce can be present as either a trivalent or tetravalent cation, and the Ce valence speciation will depend on the following model reaction:

$$Ce^{3+}O_{1.5}(fluid) + xO_2 = Ce^{4+}O_2(fluid) \quad (1)$$

where higher oxygen fugacity values drive the reaction to the right, and $x = 0.25$, assuming ideality of this reaction across all oxygen fugacity values. Since Ce^{4+} is more compatible in the Zr^{4+} site of zircon, a higher concentration of Ce in zircon is indicative of crystallization from a more oxidized fluid. It is also important to note that in natural settings, the concentration of REEs in the fluid may also fluctuate based on salinity, temperature, and the overall composition of the rock with which the fluid is interacting. To separate the component of the $D_{Ce}^{zrc/fluid}$ resulting from changes in redox state from other factors (e.g., sensitivity of D-value to T, fluid composition, charge compensating substitution mechanisms for REE^{3+}), the partition coefficients of La and Pr are used to calculate a Ce anomaly in the following manner:

$$\left(\frac{Ce}{Ce^*}\right)_D = \frac{D_{Ce}^{zircon/fluid}}{\sqrt{D_{La}^{zircon/fluid} \times D_{Pr}^{zircon/fluid}}} \quad (2)$$

The $D_{Ce3+}^{zrc/fluid}$ is not directly measurable but is calculated by quantifying both $D_{La}^{zrc/fluid}$ and $D_{Pr}^{zrc/fluid}$. The measurable quantity $D_{Ce}^{zrc/fluid}$ represents the combined partition coefficient of both Ce valence species, such that the Ce zircon-fluid partition coefficient from a single experiment represents a combination of $D_{Ce3+}^{zrc/fluid}$ and $D_{Ce4+}^{zrc/fluid}$. In principle a zircon with $(Ce/Ce^*)_D = 1$ crystallized at an fo_2 equal to or lower than some value. In other words, if the zircon Ce anomaly is equal to 1 at an fo_2 equal to the Fe-FeO (IW) equilibrium, a zircon forming at ΔIW-2 would produce the same anomaly. Thus, a Ce anomaly of 1 does not provide an absolute constraint on the fo_2 value. The valence speciation curve for Ce has a working range that is limited by the speciation curve for redox-sensitive system. At either extreme of valence speciation curve (i.e., as the system approaches 100 % Ce^{3+} or 100 % Ce^{4+}), the usefulness of a mineral oxybarometer begins to diminish in the system. Once $(Ce/Ce^*)_D$ is equal to 1, the same $(Ce/Ce^*)_D$ value will be recorded under more reducing conditions. This is because both systems exist at fo_2 conditions where Ce^{4+} concentrations in the hydrothermal-zircon system are below detectable concentrations. Similarly, there is a threshold beyond which the Ce anomaly ceases to increase because of the elevated concentration of Ce^{4+} influenced by oxygen fugacity. This case is extremely rare on Earth, though there are documented occurrences of stetindite (ideal formula $Ce^{4+}SiO_4$) in pegmatites (Schlüter et al., 2009; Trail et al., 2015).

Since Eu is either divalent or trivalent in terrestrial systems, the speciation in the fluid is expected to be governed by the following reaction:

$$EuO(fluid) + xO_2 = EuO_{1.5}(fluid) \quad (3)$$

where $x = 0.25$, assuming ideality of this reaction across all oxygen fugacity values. Trivalent Eu is significantly more compatible in the zircon structure when compared to Eu^{2+}. Like above, redox partitioning of Eu in zircon is explored relative neighboring rare earth elements by calculating the Eu anomaly:

$$\left(\frac{Eu}{Eu^*}\right)_D = \frac{D_{Eu}^{zrc/fluid}}{\sqrt{D_{Sm}^{zrc/fluid} \times D_{Gd}^{zrc/fluid}}} \quad (4)$$

where the respective D-values correspond to the REE partition coefficient between zircon and fluid. The denominator of Eq. (4) is a proxy for the Eu^{3+} partition coefficient in zircon, and the numerator is the combined Eu^{2+} and Eu^{3+} partition coefficient. The $(Eu/Eu^*)_D$ is predicted to range between 0 and 1. If only Eu^{3+} is present in the system, $(Eu/Eu^*)_D \approx 1$. If only Eu^{2+} is present in the system, and Eu^{2+} not incorporated into the zircon structure, $(Eu/Eu^*)_D \approx 0$.

3. Experimental methods and measurements

3.1. Starting mixture

All starting materials were prepared from reagent-grade mixtures of chlorides and oxides ($ZrCl_4$-$REECl_3$-SiO_2-NaCl). To evaluate the purity of the $ZrCl_4$ (99.5+ % pure, CAS: 10026-11-6) for potential rare earth element contaminants (i.e., an internal quality control check), a solution-based analysis was carried out by inductively coupled plasma mass spectrometry (ICP-MS) using the Agilent 7900 at the University of Rochester. This was done by dissolving $ZrCl_4$ in nitric acid (trace metal grade), where the solution was diluted to 2 % in 18.2 MΩ-cm H_2O. A 2 ppm REE tuning solution was produced for each REE from a 100 ppm REE stock solution supplied by Inorganic Ventures (Lot: G2-MEB499122), suspended in the same batch of 2 % nitric acid to quantify impurities. After it was established that the $ZrCl_4$ was sufficiently pure (see Supplementary Table 1, 2), we tested the purity of the REE-chlorides, which have stated purities of 99.9 %. A REE-chloride mixture was carefully prepared by weighing out aliquots of $LaCl_3$, $PrCl_3$, $CeCl_3$, $SmCl_3$, $EuCl_3$, $GdCl_3$, $DyCl_3$, $HoCl_3$, $TmCl_3$, and $LuCl_3$ using a Sartorius CPA225D balance. The synthetic REE mixture is enriched in LREEs (La, Ce, Pr), with progressively decreasing concentration for the mid to heavy REEs (e.g., $LaCl_3 \approx 19$ wt% of the total REE mixture, $EuCl_3 \approx 10$ % of the total, and $LuCl_3 \approx 2$ % of the total). This was done to account for the lower expected compatibility of the light rare earth elements in zircon, and to limit challenges with measuring the low concentrations in zircon by laser ablation inductively coupled plasma mass spectrometry (LA-ICP-MS). Approximately 1 g total of 10 REE-chlorides was thoroughly dry mixed by hand in a mortar and pestle for 60 min. Once homogenized, two different concentrations of REE chloride material were dissolved in 2 % nitric acid, for a total REE content of approximately 50 ppm and 100 ppm. We measured each by solution ICP-MS, and the calculated and measured REE concentrations are in general agreement with the expected REE pattern, though the measured values are less than the calculated values (Fig. 1). We attribute the discrepancy between the measured and calculated values to the adsorption of H_2O on the hygroscopic REE-chlorides.

Afterwards $ZrCl_4$, the REE-chloride mixture, SiO_2, $O_{18}Na_6P_6$, and ± NaCl and were well mixed in a mortar and pestle for approximately one hour. Two mixtures were prepared, differing primarily in the presence or absence of NaCl (Table 1).

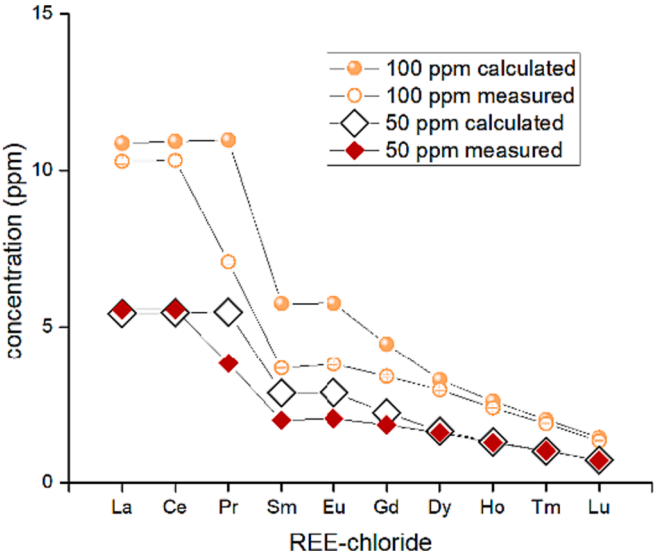

Fig. 1. The calculated weighed out quantity of REEs determined from "dry" REE weights measured on the Sartorius CPA225D balance, vs. the quantity measured by ICP-MS. Whenever feasible, REEs with an odd atomic number were added in preference to those with an even atomic number. This choice was made given the lower likelihood of background contamination from the environment due to the odd–even nucleosynthetic effect.

Table 1
Starting mix for experiments.

component	total (g) - mix1	fraction	total (g) - mix2	fraction
$ZrCl_4$	0.951	0.496	0.970	0.308
REE-Cl_3 total*	0.052	0.027	0.051	0.016
SiO_2	0.907	0.473	1.109	0.353
$O_{18}Na_6P_6$	0.009	0.004	0.009	0.003
NaCl	–		1.007	0.320
sum	1.918	1	3.146	1

* See Supplementary Table S01.

3.2. Oxygen fugacity-buffered experiments

Zircon-fluid REE partitioning experiments were performed in a piston cylinder device at 1 GPa from 1200 to 800 °C. Synthesis experiments were done instead of using zircon seeds, as hydrothermal zircon recrystallization during piston cylinder experiments is incomplete (e.g., Ayers et al., 2018; Trail et al., 2019). The fo_2 was controlled for each experiment using five different metal–metal oxide buffers. The Re-ReO_2 and Ru-RuO_2 buffers were imposed by adding the metal and complementary metal-oxide directly into the 5 mm diameter capsule. In most experiments, the capsule assembly was designed so that it could be used to impose an oxygen fugacity upon the experimental charge. For the Ni—NiO, W—WO_2, Co—CoO, buffers, a high purity (i.e., 99.9 %) bucket made of Ni/W/Co metal was machined to yield a well with an inner diameter suitable for insertion of a 5 mm diameter Pt capsule. Then, the complementary metal oxide and H_2O were added to the bottom of the metal bucket.

Afterwards, the 5 mm Pt capsule was prepared and placed inside the surrounding metal bucket. The Pt capsule tube was intentionally left longer than the depth of the bucket's well, and the extra length was carefully fashioned into a flange with a fine tipped tool around the top of the metal bucket. The Pt capsule was filled approximately 1/2 to 2/3 to the top with between 25 and 40 mg of mix 1 or mix 2. Finally, we added between 30 and 50 μL of 1 M HF to the Pt capsule. The assembled capsule components were positioned within a fired pyrophyllite bucket, with custom cut MgO cylinders placed on the top and bottom to secure the capsule at the midpoint of the graphite furnace (Fig. 2). In one

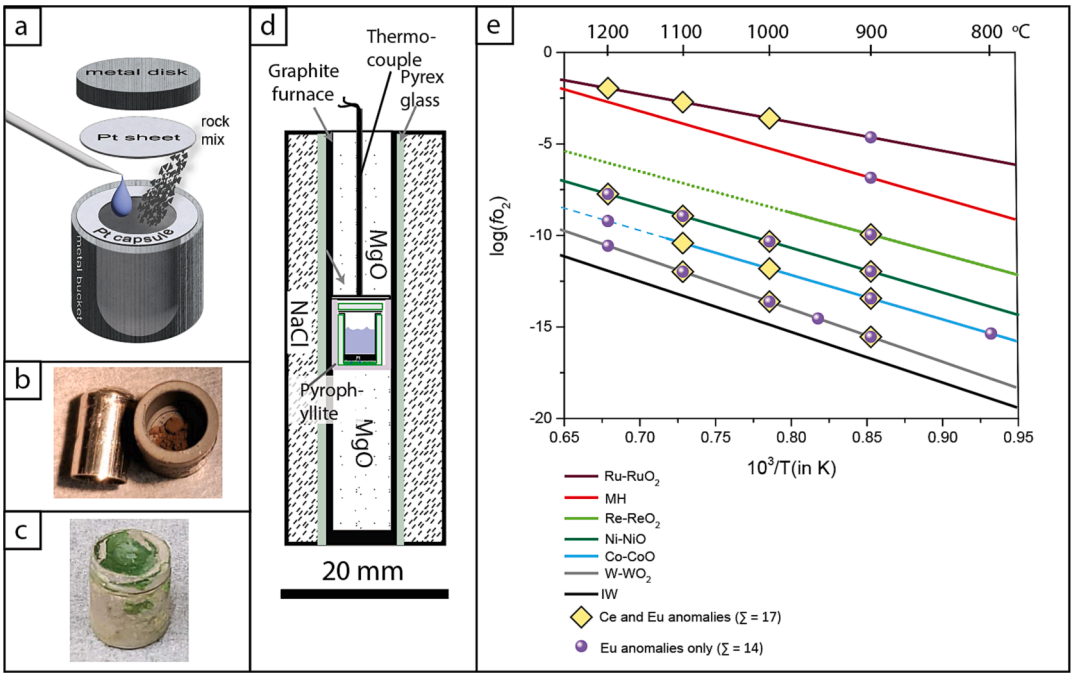

Fig. 2. (a) Illustration of the capsule design typically utilized in oxygen fugacity-buffered experiments. A 5 mm Pt capsule with a flange is inserted into the bucket and then the rock mix and fluid are added. Afterwards, a custom cut sheet of Pt is placed on top of the Pt capsule, followed by a metal disk of the same composition as the metal bucket. All pieces are inserted as a stacked unit into a pyrophyllite cup (not shown). (b) Image of Pt capsule (without the flange) sitting next to a Co metal bucket and CoO powder in the bottom. Before the Pt capsule is inserted, ~5 μL of H_2O is placed at the bottom of the metal bucket (not shown). (c) Image of a recovered capsule buffered at the Ni-NiO equilibrium; the green is NiO. (d) The experimental assembly used in almost all experiments. The outside of the NaCl cells were wrapped in Pb foil before inserting the assembly into the pressure vessel. In the sole 800 °C experiment, approximately 50 % of the length of the MgO rod below the capsule was replaced with borosilicate glass (not shown). (e) The metal–metal oxide fo_2 buffer curves shown along with experiments conducted (solid symbols). The dashed curves associated with fo_2 buffers Co-CoO and Re-ReO_2 represent extrapolation beyond the equation-of-state calibrations. The solid diamonds are experiments in which Ce and Eu anomalies were acquired, whereas solid circles represent separate experiments in which only Eu anomalies were measured. The position and slope of the lines for the metal–metal oxide reactions are defined by the equation-of-state data provided in the following studies (Fe-FeO, W-WO_2, Co-CoO, Ni-NiO, O'Neill and Pownceby, 1993; Re-ReO_2, Pownceby and O'Neill, 1994; Ru-RuO_2, O'Neill and Nell, 1997).

exception (the sole 800 °C experiment) the bottom MgO filler piece was partially replaced with borosilicate glass (Trail et al., 2009).

The samples were manually pressurized with a hand pump to 1 GPa. Once pressurized, the experiment employed a ramp rate of 200 °C/min to attain the target temperature. During the temperature ramping phase, the pressure was occasionally adjusted to attain the target pressure, until the desired temperature was reached. The temperature was measured using a 25 %WRe–3 %WRe thermocouple wire from Concept Alloys, with an accuracy of ~3 °C. Experiments were allowed to dwell for 10 to 261 h, where longer duration experiments were conducted at lower temperatures to help produce large crystals suitable for analysis. Samples were quenched to room temperature in ~1 min by stopping power to the transformer and therefore the graphite furnace. After a given experiment was removed from the pressure vessel, the Pt capsule was gently opened to expose the zircon and fluid products. We used a 10 μL micro syringe to extract fluid from each capsule, which was immediately transferred into a prepared solution of 2 % nitric acid, mixed from the same acid aliquot used to measure the starting material. Between 2 and 10 μL of fluid was recovered for each experiment. Following this step, the zircons were extracted from the capsule and cleaned in dilute HF acid to help remove quench material. The zircon fraction was mounted on double sided tape, and then cast in epoxy. In most cases, epoxy rounds were manually polished with 1 μm SiC sandpaper before being finished with colloidal silica (0.05 μm) using an automated polisher. For some experiments, especially those performed at higher temperature, cured epoxy mounts already possessed zircons with flat crystallographic facets exposed at the surface of the epoxy mount. In cases where exposed zircons were ~10 × 10 μm^2 or larger, polishing was deemed unnecessary.

3.3. Zircon analysis

Synthetic zircons were analyzed *in situ* with a Cetac Analyte G2 193 nm laser ablation (LA) system attached to the above-described ICP-MS at the University of Rochester. Epoxy mounts were loaded into the LA HelEx 2 volume chamber, and during the analysis, the He flow was set to 0.6 L/min in the chamber and 0.2 L/min in the HelEx arm. The laser energy was adjusted to 4 mJ with a laser output of 70 %, which resulted in a fluence of 4.7 J/cm^2. For each analysis, a circular spot between 3 and 15 μm (depending on grain size) was selected, and background counts were collected for 30 s, followed by 10–20 s of ablation (depending on the size of the zircon), and finally a 30 s washout period. The analyzed masses typically included ^{23}Na, ^{29}Si, ^{31}P, $\pm^{45}Sc$, ^{91}Zr, ^{139}La, ^{140}Ce, ^{141}Pr, ^{147}Sm, ^{153}Eu, ^{157}Gd, ^{163}Dy, ^{165}Ho, ^{169}Tm, and ^{175}Lu. The mass ^{23}Na was added as a proxy to check for fluid inclusions in the zircon, which is especially important for rare earth elements with a partition coefficient less than one, like La and Pr. Unknowns where quantified using NIST612 as a primary standard and ^{91}Zr was chosen as an internal standard. Data were reduced with the Iolite 3.1 software package using the preloaded X_TraceElements_IS data reduction scheme (Paton et al., 2011). We also monitored an in-house zircon standard (Kuehl Lake) believed to be from the same locality as the 91,500 zircon standard (Trail et al., 2015; 2018). Select data were reduced with both standards, and the derived concentrations of the unknowns for the two standards are typically within 15 % (Supplementary Table S02). With the exception of the above-mentioned standard comparison results presented in Supplementary Table S02, all concentrations were standardized relative NIST612. This standard has ~500 ppm of each REE, whereas with Kuehl Lake zircon, REE contents can be close to or below

the limit of detection for some LREEs and Eu when using the small spot size required to analyze the experimental zircons.

A 3 μm spot size was required to analyze some experimental zircons. This did not yield a complete REE pattern because the light rare earth elements were either below the limit of detection or inclusions were inferred due to the presence of detectable Na. In these cases, follow-up analyses were conducted with specific emphasis on extracting, at the minimum, zircon Eu anomalies. The prioritized masses were ^{147}Sm, ^{153}Eu, ^{157}Gd with the addition of ^{163}Dy, ^{165}Ho, ^{169}Tm, and ^{175}Lu in some cases. In this way, we were able to acquire partition coefficients for the mid- to heavy-REEs and Eu anomalies for some experiments. We also conducted additional analyses on zircons that contain the full complement of rare earth elements but focused only on obtaining additional Eu anomaly data for smaller zircons in the same aliquot. With this information we see no evidence for a difference in the Eu anomaly as a function of spot size or grain size.

Reflected light transmitted light, and backscattered electron (BSE) images of zircons were collected at the University of Rochester. The BSE images were collected with the Hitachi TM4000 PLUS Series – II benchtop SEM using a 15 keV accelerating voltage. Cathodoluminescence images (CL) were collected on the JEOL 8530F field emission electron probe microanalyzer at the Smithsonian National Museum of Natural History using a 15 keV accelerating voltage and a 20 nA current.

3.4. Analysis of the experimental fluid

To analyze the experimental fluids, we prepared a total of five standards with different REE concentrations. The standard set included a 2 % solution of nitric acid without rare earth elements ("Calibration blank"), and REE standards with concentrations of 10 ppb, 50 ppb, 500 ppb, and 5000 ppb of each rare earth element. These standards were prepared from a 100 ppm stock solution purchased from Inorganic Ventures (Lot: G2-MEB499122). All solutions were prepared using the same batch of trace metal grade nitric acid as the unknown samples. The key analytes were ^{139}La, ^{140}Ce, ^{141}Pr, ^{147}Sm, ^{153}Eu, ^{157}Gd, ^{163}Dy, ^{165}Ho, ^{169}Tm, ^{172}Yb and ^{175}Lu. Each of these analytes were acquired in increasing order of mass for 0.09 s, which constituted one sweep. All these masses were then recollected for a total of 100 sweeps and this process was performed thrice. We used an autosampler to uptake 1.5 mL of each of the calibration standards in increasing order of concentration. For each of the solutions, the autosampler collected fluid for 30 s using a peristaltic pump rotating at 0.5 rps (revolutions per second). This preceded a 30 s acquisition period during which the pump speed slowed down to 0.2 rps and each analyte was acquired. After the acquisition period, we rinsed the lines and the instrument for 120 s using 2 % HNO_3. In cases where experimental fluid dilutions were larger, we made 5 calibration solutions, each containing 0 ppb ("Calibration blank"), 1 ppb, 10 ppb, 100 ppb, and 1 ppm of La, Ce, Pr, Sm, Eu, Gd, Dy, Ho, Tm, Yb and Lu. In some cases, we added 2 ppb of indium to act as an internal standard, and included ^{115}In in the list of analytes, to correct for instrumental drift (Supplementary Table 3). The Agilent Masshunter software, version 4.1, was used to reduce the solution-based ICP-MS measurements once they were completed.

4. Results

Zircon sizes typically range from a couple of microns to ~ 15 μm, though grains can be as large as 100 μm. Some of the largest grains exhibit zoning as determined by cathodoluminescence imaging (Fig. 3**)**. In most cases, grains are free from obvious secondary phases. However, this is not always the case; Fig. 3c shows evidence a vapor bubble in a quartz crystal. In addition, Fig. 3h documents Si+Zr rich materials suspected to be amorphous near the crystal rim. We did not observe a systematic intragrain difference in the measured Ce/Eu anomalies. In general, the size of the crystals correlates with the experiment temperature, where larger grains were produced at higher temperature. At 900 °C and below, experiments were quartz saturated. In addition, zircon synthesized from mix 2 (NaCl-bearing) were substantially larger and easier to analyze. Because of this, $D_{REE}^{zrc/fluid}$ from mix 2 represent most of the data reported. We do however, use mix 1 partition coefficients to explore how changes in fluid composition could potentially affect zircon Ce and Eu anomalies. Unless otherwise noted, zircon Ce and Eu presented are those from experiments done with mix 2.

All zircon and fluid measurements are presented in Supplementary Tables 3 and 4, and the compiled partition coefficient dataset can be found in Supplementary Table 5. Representative plots of partition coefficient versus REE show the expected monotonic trends of increasing compatibility from La to Lu for zircon. For general context, the average $D_{La}^{zrc/fluid}$ is 0.005, $D_{Sm}^{zrc/fluid}$ is 1.3, and $D_{Lu}^{zrc/fluid}$ is 135, representing almost 5 orders of magnitude of variation from the light to heavy REEs (Fig. 4**a, b**).

It is also crucial to explore to what extent the quenched fluid is an accurate representation of the rare earth element contents at the experimental conditions. The likelihood that modification to the fluid occurs during the quench is essentially guaranteed, given the high silica content expected for these fluids at experiment conditions. For the purposes of this study the key aspect to explore is whether quenching could alter the calculated Eu or Ce anomaly. We explore this by calculating the partition coefficients calculated using: (i) the starting mix composition which are discussed in section 2.1 and presented in Supplementary Table 1 and 2 versus (ii) the recovered fluid after the quench. We make this comparison and find that the shape of the REE patterns is very similar from La to Gd, independent of whether the denominator of (i) or (ii) is used to calculate the partition coefficient (Fig. 4**c)**. Starting with Dy, some deviation in the shape of the REE pattern is more evident, where the slope defined by the Dy and heavier REEs becomes shallower for D-values calculated using approach (i) vs. the D-values derived from (ii). In making this comparison, we see very little difference between the calculated Ce and Eu anomalies as a function of the denominator used to calculate partition coefficients (i.e., (i) vs. (ii)). Thus, there is no evidence to support that quenching had a significant effect on the magnitude of the anomalies.

We also compare our results to a previous zircon-fluid REE partitioning study performed by Ayers and Peters (2018) who conducted piston cylinder experiments from 800 to 1000 °C at 1.5 GPa with the fo_2 buffered at the NNO equilibrium. In more detail, Ayers and Peters (2018) recrystallized natural zircon in aqueous fluids (H_2O, 1 m NaOH, and 1 m HCl), measured the zircons by LA-ICP-MS, and then derived $D_{REE}^{zrc/fluid}$ through mass balance calculations. The resulting partition coefficients, from light to heavy REE, cover almost 2 orders of magnitude of variation which is substantially less variation than $D_{REE}^{zrc/fluid}$ reported here (Fig. 4**d**). The $D_{REE}^{zrc/fluid}$ values reported by Ayers and Peters (2018) are incompatible (n = 70), except for $D_{Lu}^{zrc/fluid}$ values reported for two of the experiments. As noted by these authors, the anomalously high LREE contents measured in zircon are likely due to contamination with quenched solutes enriched in the LREE incompatible elements.

Table 2 provides a summary of the Ce and Eu anomalies for each experiment, along with the experimental conditions. In this table and hereafter, we only use the fluid-based measurements to calculate anomalies – i.e., approach (ii) noted above – but data are available in Supplementary Table 1 to calculate the anomalies from the starting REE-chloride abundance if desired. Then the anomalies are used to derive calibrations to quantify the oxygen fugacity of natural hydrothermal systems. The simplest and most broadly applicable calibration utilizes the Ce anomalies in zircon (Table 2), calculated using Eq. (2). We examine a few necessary assumptions before presenting a practical calibration for natural systems.

First, we assume the substitution mechanism for the trivalent REEs in zircon operates independent of fo_2. The data presented here suggest

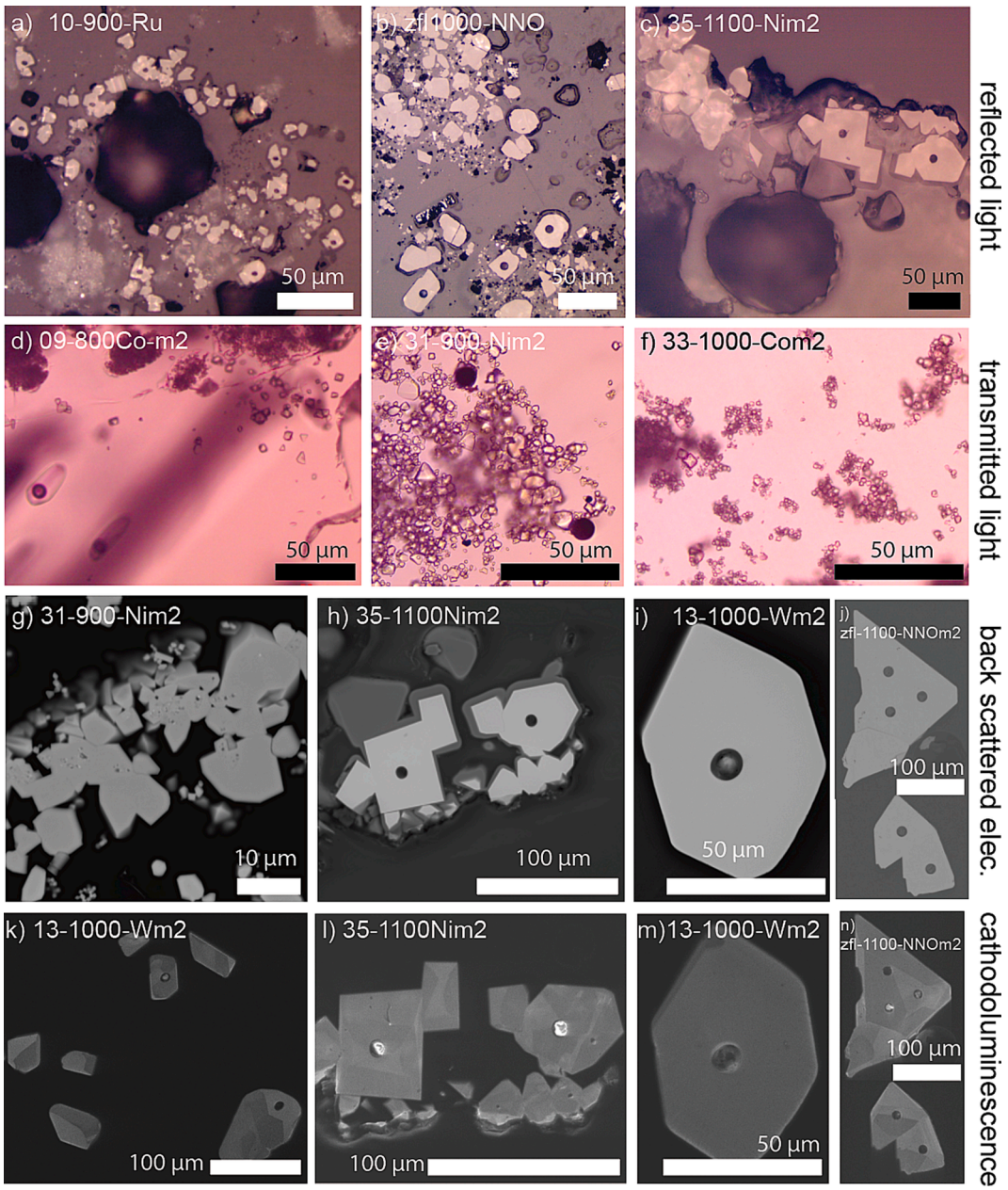

Fig. 3. Example images of the zircon products documented by reflected light (RL), transmitted light (TL), backscattered electron (BSE), and cathodoluminescence (CL) images. Grain size is positively correlated with experiment temperature. ***(a)*** RL image of zircons analyzed with a 3 µm spot. ***(b–c)*** Representative RL images of experimental zircon analyzed with 5 µm spots. ***(d)*** TL image from experiment 09-800Co-m2, where zircon is present as both a matrix phase and as inclusions in quartz. ***(e–f)*** Other TL images conducted at higher temperature show grains that approach 15 µm. ***(g)*** Backscattered electron images of grains reveal some very small (<1 µm) unreacted ZrO_2 inclusions in zircons grown at 900 °C. This image represents an example as to why analyzing smaller grains from 800 and 900 °C experimental products presented challenges. ***(h–j)*** The other grains shown in the same row (1000 and 1100 °C) are larger, and do not show unreacted features observed at lower T. (***k-n***) Representative CL images of some of the largest grains encountered show evidence for zoning. The bright circles seen in some of the images are the locations of the LA spots.

that, outside of the ionic radii differences of the trivalent REEs, there is no significant fractionation process in the systems investigated here. We also assume that the zircon Ce anomaly will not depend on changes to the partition coefficients or substitution mechanisms of the trivalent REEs. That said, it is difficult to independently constrain these parameters for each experiment via element chemical concentration measurements of the fluid and zircon, and the entry of trivalent REE into zircon could involve a coupled substitution with P ($REE^{3+} + P^{5+} \rightarrow Zr^{4+} + Si^{4+}$) and/or H ($REE^{3+} + H^{+} \rightarrow Zr^{4+}$), both of which have been observed in natural and experimental systems (Hanchar et al., 2001; Trail et al., 2011b; Burnham and Berry, 2012; de Hoog et al., 2014; Chowdhury et al., 2020). We allow for some variation by letting the constant of 0.25 (see Eq. (1)) vary in our empirical fitting (e.g., Tailby et al., 2023). We also consider that changes in temperature could result in variations in the partition coefficient, which, in turn, could affect the magnitude of the zircon Ce anomaly. Previous studies have documented the sensitivity of the partition coefficient to temperature (e.g., Drake and Weil, 1975; Watson and Green, 1981; Liang et al., 2013; Chowdhury et al., 2023).

With this framework, the Ce anomaly is calculated from the partition coefficient data using Eq. (2), and the following empirical fit is used:

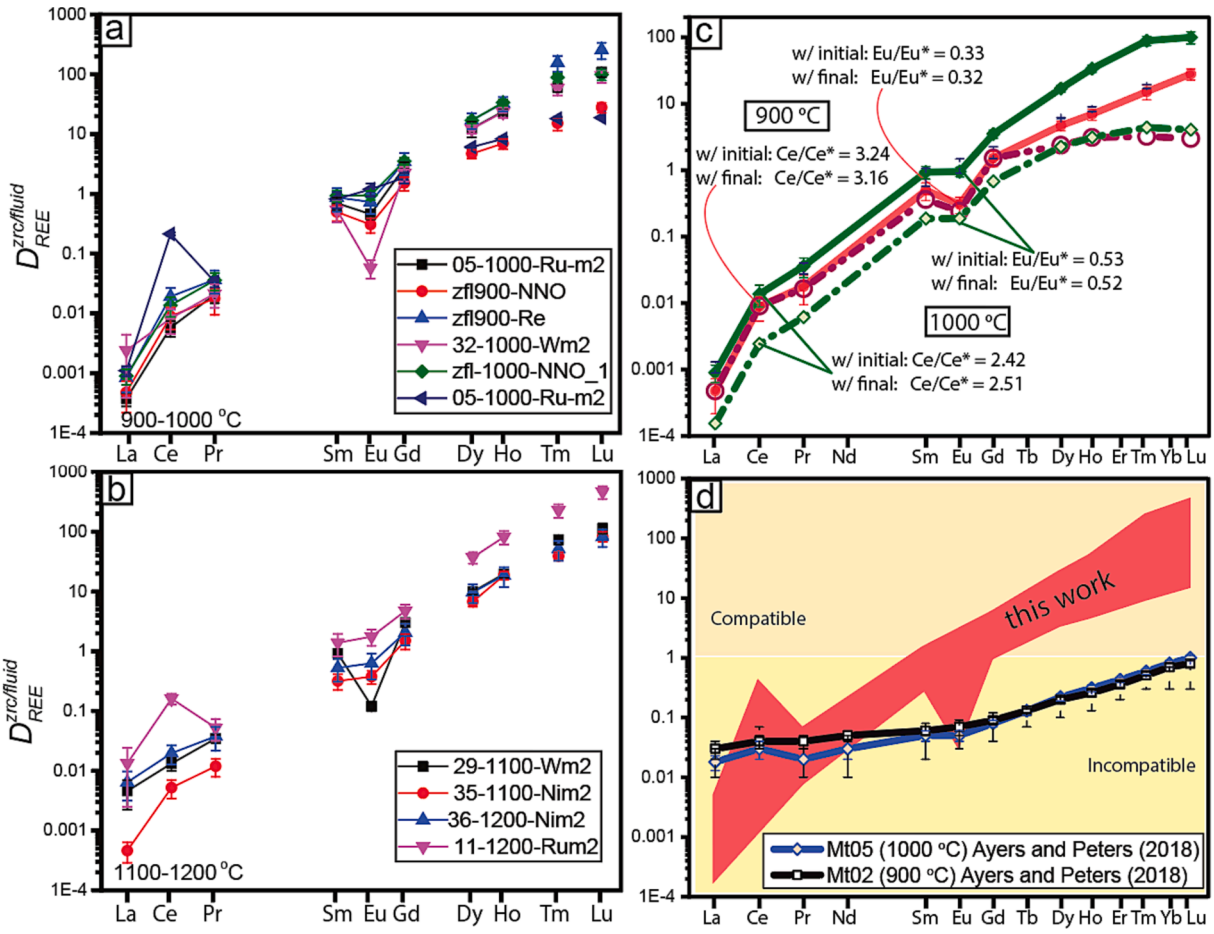

Fig. 4. (a,b) Example zircon-fluid partition coefficients and REE patterns for select experiments. In all experiments the non-redox sensitive REEs show a monotonic pattern of increasing compatibility from La to Lu. See Supplementary Table 5 for data used to produce these graphs. (c) A comparison of the partition coefficients calculated using: (i) starting mix composition (Supplementary Table S01 and S02); vs. (ii) the recovered fluid after the quench. For both methods, the shape of the REE patterns is very similar from La to Gd, as are the calculated Ce/Eu anomalies, the latter of which are compared on the figure. Starting with Dy, deviation between the two methods is more evident. (d) Comparison of the REE patterns from this work with representative REEs patterns reported in Ayers and Peters (2018). Rare earth elements heavier than Eu tend to be compatible in the data presented here whereas virtually all $D^{zrc/fluid}_{REE}$ reported by Ayers and Peters (2018) tend to be incompatible.

$$log\left[\left(\frac{Ce}{Ce^*}\right)_D - 1\right] = (0.237 \pm 0.040) \times log(fo_2) + \frac{9437 \pm 640}{T(K)} - 5.02 \pm 0.38 \quad (5a)$$

which yields an $R^2 > 0.95$, which can be rearranged to:

$$log(fo_2) = \frac{log\left[\left(\frac{Ce}{Ce^*}\right)_D - 1\right] - \frac{9437 \pm 640}{T(K)} + 5.02 \pm 0.38}{(0.237 \pm 0.040)} \quad (5b)$$

If $(Ce/Ce^*) = 1$, this implies an absence of Ce^{4+} in the system. In this situation, the fo_2 is not directly quantifiable, though a maximum value can be inferred. The calibration curves using Eq. (5a) and the data from Table 2 are shown in Fig. 5.

While Ce anomalies are temperature dependent, Eu anomalies in zircon do not appear to show the same systematic behavior (Table 2; Fig. 6). The Ni-NiO and Co-CoO buffered experiments exhibit no obvious trend with oxygen fugacity, whereas the W-WO_2 buffered experiments have a subtle trend towards larger negative anomalies with lower temperature. And finally, the Ru-RuO_2 buffered experiments show Eu anomalies in zircon that subtly increase with decreasing T, though the basis for this statement relies heavily on the 1200 °C Ru—RuO_2 data point, rather than the other 5 data presented for temperatures that range from 1100 to 900 °C. Taking the above observations into consideration, including the absence of a temperature trend for Co—CoO and Ni—NiO, we do not include temperature as a variable to fit the experimental data.

To fit the data, we define the equilibrium constant (K) for Eq. (3) as:

$$K = \frac{a^{Eu3+}_{fluid}}{a^{Eu2+}_{fluid}(fo_2)^{0.25}} \quad (6)$$

where a^{Eu3+}_{fluid} and a^{Eu2+}_{fluid} are the activities of Eu ions in the fluid. Representing the activities as the ion concentration multiplied by the activity coefficient (e.g., $a^{Eu3+}_{fluid} = [Eu]^{3+}_{fluid} \times \gamma^{Eu3+}_{fluid}$), taking the logarithm of both sides of Eq. (6), and rearranging gives:

$$log\frac{[Eu]^{3+}_{fluid}}{[Eu]^{2+}_{fluid}} = [\log(K) - log\frac{\gamma^{Eu3+}_{fluid}}{\gamma^{Eu2+}_{fluid}}] + 0.25 \times log(fo_2) \quad (7)$$

Assuming that $\sum[\mathrm{Eu}]_{\mathrm{fluid}} = [Eu]^{3+}_{fluid} + [Eu]^{2+}_{fluid}$, and letting $z = [log(K) - log\frac{\gamma^{Eu3+}_{fluid}}{\gamma^{Eu2+}_{fluid}}]$ means that then Eq. (7) can be rearranged to yield:

$$\frac{[Eu]^{3+}_{fluid}}{\sum[Eu]_{fluid}} = \frac{1}{1 + 10^{z-(x)*log(fo_2)}} \quad (8)$$

Table 2
Experimental conditions and corresponding Ce/Eu anomalies.

Exp_ID	mix ID	T (°C)	t(h)	Buffer	log (fo_2)	ΔFMQ	$(Ce/Ce^*)_D$	$(Ce/Ce^*-1)_D$	1 s. d.	$(Eu/Eu^*)_D$	1 s. d.	# analyses	# analyses, [(Eu/Eu*) only]
09-800Co-m2	2	800	168	Co-CoO	−15.36	−0.62	–	–	–	0.28	0.03	–	7
18-900-Wm2	2	900	124	W-WO_2	−15.54	−2.77	1.35	0.35	0.22	0.05	0.01	–	7
900-CoCoO	2	900	261	Co-CoO	−13.44	−0.67	2.07	1.07	0.16	0.34	0.02	5	13
zfl900-NNO	2	900	88	Ni-NiO	−11.96	0.81	3.24	2.24	0.47	0.35	0.02	21	–
31-900-Nim2	2	900	117	Ni-NiO	−11.96	0.81	–	–	–	0.57	0.07	–	10
zfl900-Re	2	900	100	Re-ReO_2	−9.95	2.82	3.46	2.46	0.14	0.45	0.08	3	16
23-900HM	2	900	72	Fe_3O_4-Fe_2O_3	−6.85	5.92	–	–	–	0.88	0.16	–	12
04-900-Ru-m2	2	900	72	Ru-RuO_2	−4.64	7.32	–	–	–	0.96	0.07	–	27
10-900-Ru	2	900	72	Ru-RuO_2	−4.64	7.32	–	–	–	1.07	0.03	–	40
30-900-Rum2	2	900	118	Ru-RuO_2	−4.64	7.32	–	–	–	1.02	0.07	–	22
zfl-900-Re-MIX01	1	900	100	Re-ReO_2	−9.95	2.82	–	–	–	0.84	0.04	–	–
zfl-950-W-MIX1	1	950	96	W-WO_2	−14.54	−2.64	–	–	–	0.09	0.03		9
13-1000-Wm2	2	1000	67	W-WO_2	−13.61	−2.51	1.35	0.35	0.11	0.09	0.01	17	–
32-1000-Wm2	2	1000	95	W-WO_2	−13.61	−2.51	1.37	0.37	0.45	0.05	0.01	12	–
33-1000-Com2	2	1000	95	Co-CoO	−11.81	−0.71	1.66	0.66	0.60	0.21	0.02	16	–
zfl-1000-NNO	2	1000	95	Ni-NiO	−10.33	0.77	2.41	1.41	0.52	0.53	0.02	22	–
28-1000-NNO	2	1000	69	NiNiO	−10.33	0.77	–	–	–	0.43	0.08	–	12
05-1000-Ru-m2	2	1000	100	Ru-RuO_2	−3.60	7.50	35.43	34.43	2.11	0.97	0.03	2	14
zfl-1000-W-MIX1	1	1000	96	W-WO_2	−13.61	−2.51	1.41	0.41	0.07	0.02	0.00	8	–
19-1100-Wm2	2	1100	48	W-WO_2	−11.98	−3.04	–	–	–	0.09	0.00		
29-1100-Wm2	2	1100	47	W-WO_2	−11.98	−2.31	1.11	0.11	0.16	0.07	0.01	13	–
08-1100-Co-m2	2	1100	40	Co-CoO	−10.42	−0.76	1.26	0.26	0.14	0.18	0.01	8	4
zfl-1100-NNOm2	2	1100	42	Ni-NiO	−8.93	0.73	2.13	1.13	0.29	0.37	0.02	12	–
35-1100-Nim2	2	1100	47	Ni-NiO	−8.93	0.73	2.26	1.26	0.38	0.55	0.04	12	–
1100-Ru-m2	2	1100	43	Ru-RuO_2	−2.72	6.95	19.28	18.28	2.90	0.93	0.04	16	–
zfl-1100-Ni-MIX1	1	1100	48	Ni-NiO	−8.93	0.73	–	–	–	0.69	0.02		
12-1200-Wm2	2	1200	12	W-WO_2	−10.57	−2.83	–	–	–	0.16	0.02	–	30
34-1200-Com2	2	1200	10	Co-CoO	−9.21	−1.48	–	–	–	0.25	0.01	–	27
06-1200Ni-m2	2	1200	12	Ni-NiO	−7.74	0.00	–	–	–	0.61	0.06	–	12
36-1200-Nim2	2	1200	10	Ni-NiO	−7.73	0.68	1.36	0.36	0.29	0.59	0.08	20	–
11-1200-Rum2	2	1200	12	Ru-RuO_2	−1.96	6.45	7.87	6.87	3.44	0.70	0.10	21	–

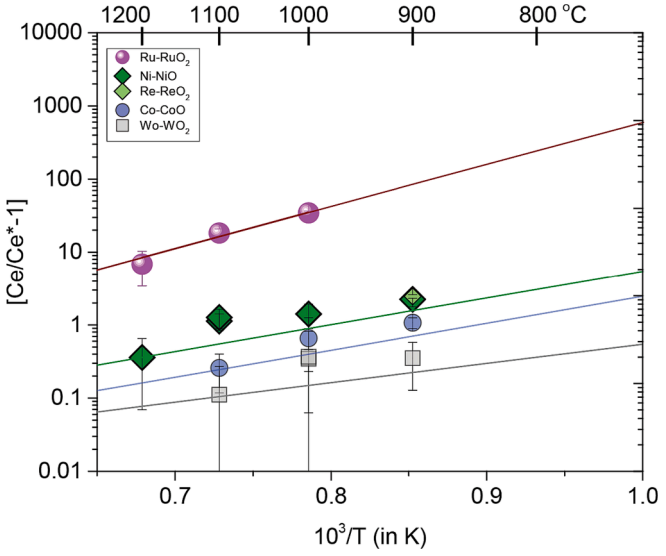

Fig. 5. Experimental calibration showing zircon Ce anomalies (plotted as Ce/Ce*−1) for zircon-fluid REE partitioning from 16 experiments using five different metal–metal oxide fo_2 buffers (Table 2). Cerium anomalies are positively correlated with fo_2 and inversely correlated with temperature such that the data exhibit well defined trends from 900 to 1200 °C. Due to the challenges of growing zircons that are large enough at low T, any application of these data and the resulting calibration will likely require extrapolation beyond the temperature range of the experiments.

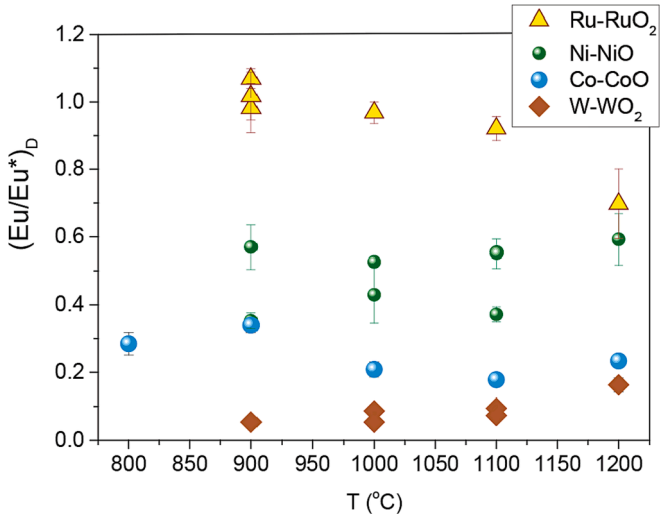

Fig. 6. Zircon-fluid Eu anomalies plotted as a function of temperature (800–1200 °C). The Eu anomalies were calculated using the D-values for Sm, Eu, and Gd. While our experiments show a clear dependence on fo_2, there is no obvious and systematic temperature dependence like that for Ce (Fig. 5). Eu anomalies in zircon have a theoretical range from 0 to 1, where a system that contains only Eu^{3+} will result in a zircon with an anomaly of 1. On the other hand, if it is assumed the system only contains Eu^{2+}, $D_{Eu}^{zrc/fluid}$ is 0, meaning the Eu anomaly of a zircon growing in this system also approaches 0.

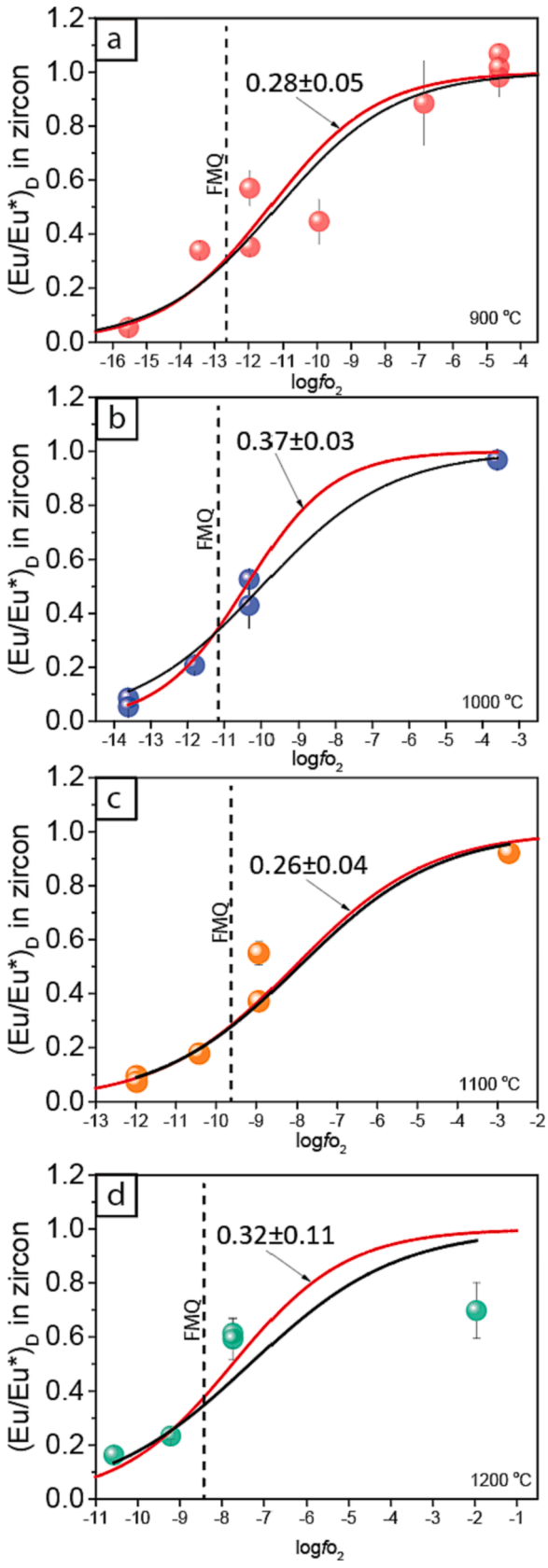

Fig. 7. (a,b,c,d) Fits to data obtained from zircon-fluid experiments of this study using Eq. (11), where Eu anomalies at temperatures of 1200, 1100, 1000 and 900 °C are shown separately. The black curves represent fits in which x is fixed at 0.25, whereas the red curves allow x to vary through the fitting procedure. When x is allowed to vary during the fit, the value is provided in the plot.

where $x = 0.25$. To relate this information to zircon, we assume that only Eu^{3+} is structurally accommodated by the zircon because of: (i) the charge mismatch between Eu^{2+} and Zr^{4+}; and (ii) the ionic radius $^{VIII}Eu^{2+}$ (1.25 Å) is a large enough mismatch relative to $^{VIII}Zr^{4+}$ (0.84 Å) such that the compatibility of Eu^{2+} in zircon can be largely excluded. Making this assumption, the fraction of Eu^{3+} in the fluid can be calculated from a zircon Eu anomaly:

$$\left(\frac{Eu}{Eu^*}\right)_D = \frac{D_{Eu}^{zrc/fluid}}{\sqrt{D_{Sm}^{zrc/fluid} \times D_{Gd}^{zrc/fluid}}} = \frac{\frac{[Eu]^{3+}_{zrc}}{\sum [Eu]_{fluid}}}{\frac{[Eu]^{3+}_{zrc}}{[Eu]^{3+}_{fluid}}} \quad (9)$$

If the denominator of Eq. (9) can be assumed to be a valid approximation for $D_{Eu3+}^{zrc/fluid}$, the Eu anomaly in zircon is approximately equal to the ratio of Eu^{3+} to total Eu content of the fluid, that is:

$$\left(\frac{Eu}{Eu^*}\right)_D = \frac{[Eu]^{3+}_{fluid}}{\sum [Eu]_{fluid}} \quad (10)$$

Substituting Eq. (10) into Eq. (8), gives the following:

$$\left(\frac{Eu}{Eu^*}\right)_D = \frac{1}{1 + 10^{z-(x)*log(fo_2)}} \quad (11)$$

Equation (11) describes the formula that can be used to calculate the oxygen fugacity in a fluid based on the zircon Eu anomaly. We present the results for each *T,* with two styles of fits compared (Fig. 7**a–d**). The first method treats *x* in Eq. (11) as fixed at 0.25, whereas the second allows *x* to vary during the fit. All temperatures agree for two different fitting methods, with the exception of the 1000 °C set of experiments. In this scenario, when *x* is allowed to vary, the result is $x = 0.37 \pm 0.03$. The cause of this discrepancy is not readily apparent.

Given the lack of evidence for a T-dependent trend in these data, there is the opportunity to fit all the data independent of temperature. To do this, we introduce the following modification to Eq. (11):

$$\left(\frac{Eu}{Eu^*}\right)_D = \frac{1}{1 + 10^{[z-(x)\times\Delta FMQ]}} \quad (12)$$

Equation (12) expresses all data relative to the FMQ buffer, independent of temperature, such that the difference from the FMQ equilibrium reaction is used in place of log (fo_2). For example, $\log_{FMQ}(fo_2)$ at 1100 °C is, $10^{-9.7}$ and at 900 °C it is $10^{-12.8}$. The $\log_{NiNiO}(fo_2)$ values at 1100 °C and 900 °C are $10^{-8.9}$ and 10^{-12} respectively. The ΔFMQ of NiNiO at 1100 °C and 900 °C = 0.8 in both cases, making these two values easier to compare without treating temperature. In light of the observation that different metal–metal oxide buffer curves are ~parallel in 1/T-log(fo_2) (Fig. 2c), there will be little or no difference in ΔFMQ with temperature. Once ΔFMQ is calculated the 27 experiments are fit to Eq. (12), with *x* and *z* allowed to vary during the fitting, to yield:

$$\left(\frac{Eu}{Eu^*}\right)_D = \frac{1}{1 + 10^{[0.30\pm0.04 - (0.27\pm0.03)*\Delta FMQ]}} \quad (13a)$$

Or rearranged to:

$$\Delta FMQ = \frac{0.30 \pm 0.04 - log\left[\frac{1}{\left(\frac{Eu}{Eu^*}\right)_D} - 1\right]}{0.27 \pm 0.03} \quad (13b)$$

with an $R^2 = 0.92$. The results of this fit to Eq. (13a) are shown in Fig. 8.

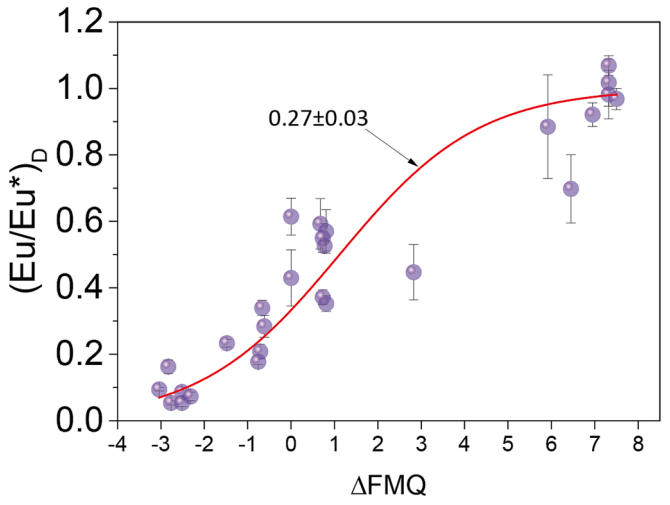

Fig. 8. Zircon $(Eu/Eu^*)_D$ for all temperatures from 27 experiments conducted between 800 and 1200 °C are plotted relative to the FMQ equilibrium buffer. The curve is the result of fitting these data using Eq. (12), with the constants of the fit provided in Eq. (13a). Fits for individual temperatures can be found in Fig. 7.

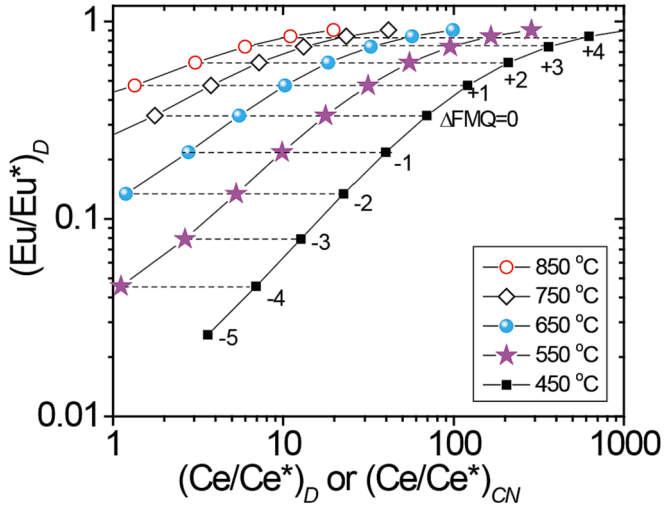

Fig. 9. Correlative Eu and Ce anomalies for a given oxygen fugacity and temperature using Eqs. (5) and (13a). We expect that most fluids will have Eu anomalies, and therefore application of this redox concordia diagram will require direct quantification of the fluid composition that was contact with the zircon when it formed.

5. Discussion

The experimentally derived calibrations in Eqs. (5) and (13a) represent a new method to assess oxygen fugacity values of high temperature fluids. Possible applications are numerous. Their application, for example, could help characterize the changes in redox conditions of fluids that drive precipitation of critical minerals (e.g., late stage pegmatitic fluids or greisens; Blevin, 2004). They also present an opportunity to explore the interaction between different hydrothermal systems, particularly in environments when vastly different redox conditions interact; i.e., where magmatic and meteoric fluids meet and mix, including ore-forming environments (Schaltegger et al., 2005; Pelleter et al., 2007; Toscano et al., 2014; Fu et al., 2009; Yang et al., 2013; Li et al., 2014; Möller and Williams-Jones, 2017; Jiang et al., 2019; Li et al., 2022; Nazari-Dehkordi and Robb, 2022; Walsh and Spandler, 2023).

These calibrations also allow for the investigation of redox evolution in a system transitioning from magmatic to a late-stage hydrothermal environment. Zircons from the Mole Granite in New South Wales, Australia, for instance, represent an excellent natural laboratory to investigate the redox evolution from the silicate melt to the fluid/vapor saturated conditions. Once fluid/vapor saturation has occurred, the fo_2 is especially subject to large changes in the relative fo_2 evolution that can be difficult to predict. Previous studies from Mole Granite show that igneous zircons exhibit smaller Ce anomalies than the HT zircons, possibly indicative of a higher oxygen fugacity as the system evolved (Pettke et al., 2005). The opposite trend is found in the Boggy Plain Zoned Pluton in eastern Australia in which the Ce anomaly is less pronounced in the lower T hydrothermal system, implying a lower oxygen fugacity than the igneous system (Hoskin, 2005). Additionally, our results could be utilized to investigate the fluid oxygen fugacity during fluid-rich crustal metamorphism or subduction zone processes (e.g., Hoskin and Black, 2000; Harley et al., 2007; Rubatto, 2017).

In the sections that follow, we broaden the context of our experimental data by exploring the complementarity of correlative Ce/Eu anomalies at a given T and fo_2 (section 5.1), other methodologies for calculating Ce/Eu anomalies though application of the lattice strain model (section 5.2), and evidence for zircon anomaly variation as a function of the fluid salinity (section 5.3). Finally, we apply our results to natural systems that meet specific criteria (section 5.4).

5.1. Correlative Ce and Eu anomalies

Equations (5) and (13) depict two independent calibrations that, in theory, could be utilized in conjunction as a redox concordia diagram (Fig. 9). Much like a U-Pb concordia diagram, the curves presented in Fig. 9 represent agreement between Ce and Eu anomalies in zircon for a given T and oxygen fugacity. In this figure, the Ce/Eu anomalies are calculated via the partition coefficients. However, in natural systems where the fluid composition cannot be measured, Ce/Eu anomalies in zircon are generally calculated relative to a chondrite normalized reservoir (CN). If this is the sole method available for calculating the anomalies in a natural system, the following assumptions must be made:

$$(Ce/Ce^*)_D \approx (Ce/Ce^*)_{CN} \quad (14a)$$

and,

$$(Eu/Eu^*)_D \approx (Eu/Eu^*)_{CN} \quad (14b)$$

If the assumptions hold, this means that there are no Eu and Ce anomalies in the fluid. In this case $(Ce/Ce^*)_{CN}$ from natural zircon can be directly substituted for $(Ce/Ce^*)_D$ in Eq. (5). As shown and discussed elsewhere, Eq. (14a) is a reasonable approximation for silicate melts (Thomas et al., 2002; Reid et al., 2010; Trail et al., 2011a; Trail et al., 2012), though to our knowledge this approximation has not been tested for hydrothermal zircon-bearing systems. Since major rock-forming minerals in subsolidus/hydrothermal systems that sequester Ce relative to La and Pr are rare or altogether absent, Eq. (14a) is likely to be a valid approximation in most cases. Exceptions to this may be very oxidized pegmatite systems in which extreme levels of trace element enrichment can give rise to rare Ce^{4+}-rich minerals (e.g., stetindite, $Ce^{4+}SiO_4$; Schlüter et al., 2009), mineral solubility and stability reactions that depend on fo_2, (Trail, 2018; Trail and Wang, 2008; Schmidt et al., 2021) or REE-rich ferromanganese crusts where both negative and positive Ce anomalies are observed in systems proximal to ocean floor hydrothermal fields (Plank and Langmuir, 1998; Mills et al., 2001).

Conversely, it is improbable that Eq. (14b) can be assumed to be applicable in most cases because it is well-documented that major rock-forming minerals fractionate Eu from Sm and Gd (e.g., plagioclase feldspars, pyroxenes, and amphibole; Drake and Weill, 1975; Shearer et al., 2006; Karner et al., 2010; Li et al., 2018). The crystallization of a major rock-forming phase that fractionates Eu relative to other REE has

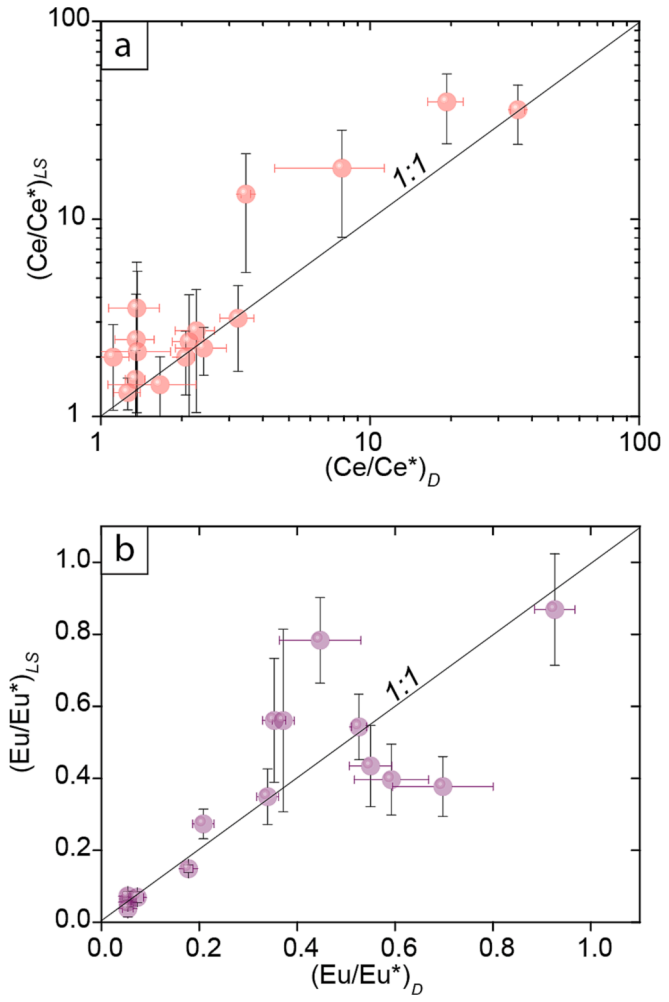

Fig. 10. (a,b) Comparison of the anomalies using Eqs. (2) and (4) (subscript 'D') vs. the anomalies calculated by the lattice strain method (subscript 'LS'); see eq (15). The lattice strain fits are used to calculate Ce* or Eu* in place of the denominators of Eqs. (2) and (4), which rely on bracketing REEs. The calculations are only provided for experiments in which 8 non-redox sensitive REEs were measurable. For experiment 05–1000-Ru-m2 the $(Eu/Eu^*)_{LS}$ is calculated to be ~ 2, and is not shown on (b).

potential to significantly modify the Eu anomaly of the growth medium. However, the Eu/Eu* and Ce/Ce* in the growth medium could be directly determined by targeting well-preserved fluid inclusions within zircon to calculate the oxygen fugacity using the two calibrations. It is also possible that fluid inclusions encapsulated in larger phases, like quartz, could be used in geologic systems that are well known to produce hydrothermal zircons such as pegmatites (e.g., Soman et al., 2010; Zhai et al., 2022). Considering that LA-ICP-MS analysis of trace elements in fluid inclusions within natural systems is now standard, this approach shows promise (Audétat, 2019). It offers additional benefits for Eu anomalies in zircon specifically, as it eliminates the need to calculate temperature to derive a relative oxygen fugacity value.

5.2. *Anomalies using the lattice strain model and light REE enrichment in zircon*

The simplest fo_2 calibrations to study redox behavior in hydrothermal zircon are based on zircon Eu/Ce anomalies calculated using adjacent REEs. It is also possible to calculate the anomalies using a different approach that involves the 8 non-redox sensitive REE partition coefficients quantified here (La, Pr, Sm, Gd, Dy, Ho, Tm, Lu). We use the lattice strain (LS) model (Blundy and Wood, 2003) to fit each individual

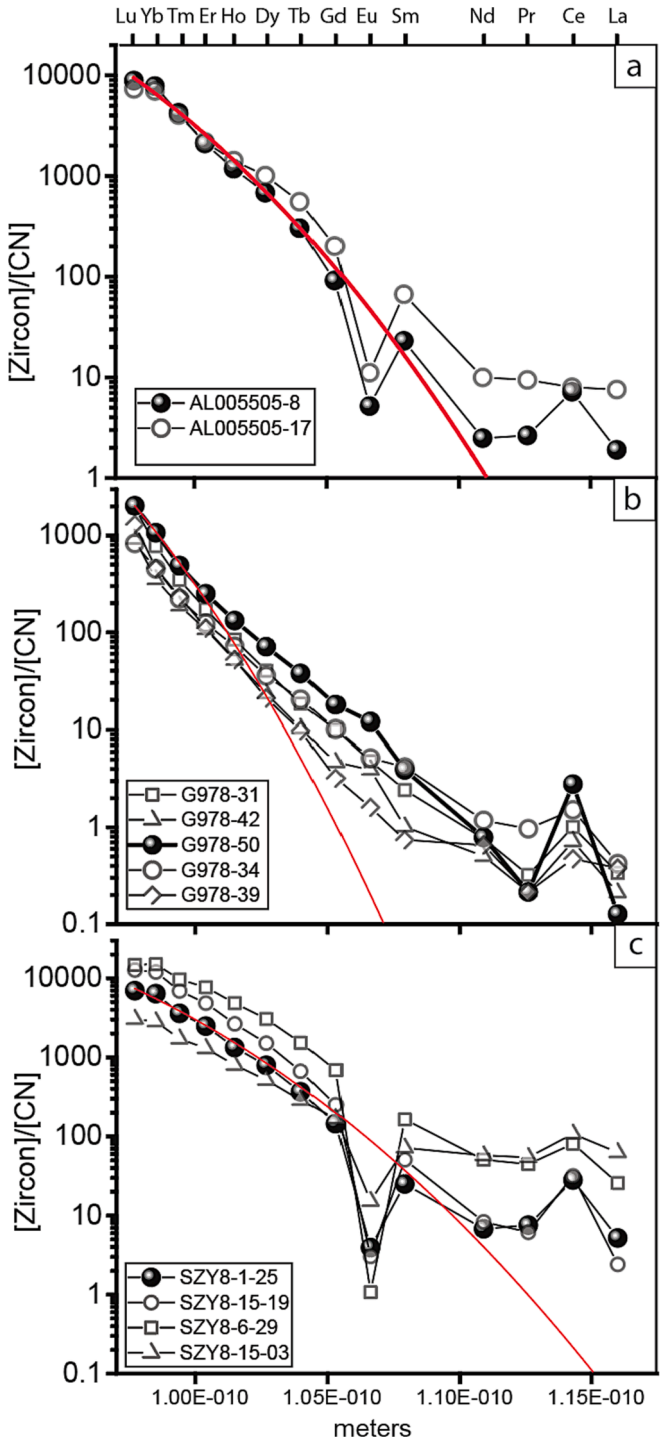

Fig. 11. Chondrite normalized REE patterns for (a) Li et al. (2023), (b) Lei et al. (2016), and (c) Jiang et al. (2019), where REEs are plotted against the ionic radii (Shannon, 1976). Enrichment of LREEs compared to middle and heavy REEs is a common occurrence in natural hydrothermal zircon, which creates complications when utilizing the lattice strain model approach to calculate Ce and Eu anomalies. The red line for each of the three plots signifies the attempt to use the lattice strain model to fit the REE data shown in solid symbols. In all cases, the apparent Ce* values are well less than predicted from La_{CN} and Pr_{CN}.

zircon REE partition coefficient pattern (n = 208 for 16 experiments, average 13 per experiment). The result of this fitting process yields the Young's modulus (Y), and the partition coefficient for the ideal radius (D_o). The Young's modulus and D_o for each of the 208 fits can be found in Supplementary Table 5. We then use this information to calculate the

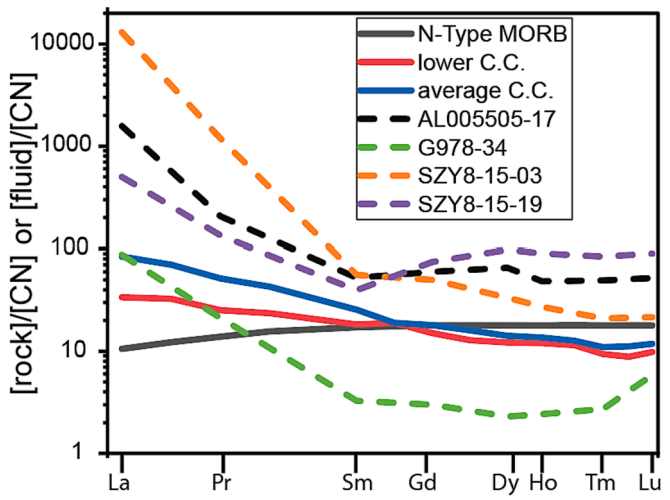

Fig. 12. Chondrite normalized (CN) silicate rock data for the upper and lower continental crust (C.C.), and N-type MORB, compared to the calculated CN fluid compositions (dashed lines). Chondrite normalization and N-Type MORB REE values are from Sun and McDonough (1989) and continental crust data are from Rudnick and Gao (2003). The REEs are demarked according to REE ionic radii, and only the non-redox sensitive data for the fluid contents are plotted. The non-redox sensitive D-values were calculated by taking the average of all experiments, the results of which were then applied to representative zircon data from Fig. 11 to derive the fluid concentration.

Ce and Eu anomalies for each zircon measurement. First, we calculate $[D_{Ce3+}^{zrc/fluid}]_{LS}$ and $[D_{Eu3+}^{zrc/fluid}]_{LS}$ using the lattice strain results. Then, we use the following equations:

$$\left(\frac{Ce}{Ce^*}\right)_{LS} = \frac{D_{Ce}^{zrc/fluid}}{[D_{Ce3+}^{zrc/fluid}]LS} \tag{15a}$$

$$\left(\frac{Eu}{Eu^*}\right)_{LS} = \frac{D_{Eu}^{zrc/fluid}}{[D_{Eu3+}^{zrc/fluid}]LS} \tag{15b}$$

Here, the numerator is the measured partition coefficient and is the same as the numerator of Eqs. (2) and (4). For each experiment, we take the average and the standard deviation of the Eu/Ce anomalies from individual zircons. The anomalies derived for each experiment are provided in Supplementary Table 6. The results of Ce and Eu anomalies calculated with Eq. (15a), (15b) and Eqs. (2), (4) show broad agreement, though some variation is evident (Fig. 10).

The experimental zircon-hydrothermal fluid data sets were fit with the previously used functional forms – Eq. (5a) for Ce and Eq. (13a) for Eu – to recalculate the constants for the fits. This yields the following calibrations:

$$log\left[\left(\frac{Ce}{Ce^*}\right)_{LS} - 1\right] = (0.22 \pm 0.01) \times log(fo_2) + \frac{7196 \pm 1022}{T(K)} - 3.249 \pm 0.77 \tag{16}$$

and

$$\left(\frac{Eu}{Eu^*}\right)_{LS} = \frac{1}{1 + 10^{0.52 \pm 0.09 - (0.24 \pm 0.07) * \Delta FMQ}} \tag{17}$$

Equations (16) and (17) may be better suited for some subsolidus systems, though in general we prefer the calibration presented in section 3 because grains of subsolidus origin often exhibit significant LREE enrichment above what would be predicted by the lattice strain parabola (e.g., Manning et al., 2006; Trail et al., 2007). Such deviation causes significant errors in the calculated $[D_{Ce3+}^{zrc/fluid}]_{LS}$ especially. To show this graphically, we review three separate studies in which zircons formed under subsolidus conditions. Li et al. (2023) identified hydrothermal zircon from the Ailao Shan-Red River shear zone (Southeast Asia) originally derived from a granitic pegmatite. Similarly, Lei et al. (2016) also identified hydrothermal zircons that were formed as overgrowths on igneous zircons because of precipitation and recrystallization in a subduction zone jadeitite from Myanmar. Finally, Jiang et al. (2019) were able to use subsolidus hydrothermal zircons to quantify the trace element content of post-magmatic fluids from the Shizhuyuan W-Sn-Mo-Bi metallic deposit in the Nanling Range, thereby qualifying the mineralization capacity of such fluids. The data from these papers are presented, along with attempts to fit one REE pattern in each set (black symbols) using the lattice strain model (Fig. 11). The LS fits show substantial deviation for the measured light REE content.

In cases like those shown in Fig. 11, the apparent Ce anomaly is orders of magnitude different when the lattice strain model approach is used in place of the bracketing La and Pr approach of Eq. (2). Therefore the application of the LS approach, at least for the zircons presented here, is likely to result in erroneous fo_2 estimate.

The LREE deviations from the lattice strain model predictions are common for hydrothermally crystallized zircon (e.g., Hoskin, 2005). However, it is not clear to what extent LREE zircon contents are due to LREE enrichment in the fluid relative to the mid-to-heavy REEs or are related to analyte contamination. More evolved felsic rocks tend to be LREE enriched relative to the MREE and HREE, and it is reasonable to expect that fluids derived from felsic magmas will also be LREE enriched. We apply the REE partition coefficient data collected here to representative zircons in the abovementioned studies (Fig. 11) to infer the fluid content (Fig. 12). The calculated (chondrite normalized) fluids – shown along with silicate systems for context – have strong enrichments in the LREEs if the reported zircon REE values are primary.

Alternatively, the reported REEs are a mixture of zircon structural constituents and contamination. The data shown in Fig. 11 assume the analyte only contains material structurally bound within the zircon structure. Any mixed analyte, be this mineral inclusion, fluid inclusion or some combination therein, will lead to a zircon REE profile that has some capacity to deviate from lattice strain parabola (Fig. 11). Fluid precipitated zircons can exhibit spongey-like textures and often contain inclusions (e.g., Fu et al., 2010). Also, if analytical regions included metamict zones, this could also impact the apparent zircon chemistry. Bell et al. (2016) developed an empirical calibration to evaluate altered igneous zircons based on the relative enrichment of LREEs to mid-REEs, though we do not consider this tool to applicable to outside of igneous systems.

Additionally, because the light to mid-REE enrichment so common in fluid precipitated zircon, a calibration that attempts to parameterize the fo_2 in terms of a mid-REE vs. Ce (e.g., Sm/Ce) will have uncertainties that are difficult to quantify in natural systems; i.e., to be accurate, $(Sm/Ce)_D$ would need to be roughly equal to $(Sm/Ce)_{CN}$, analogous to Eq. (14a). Despite the difficulties measuring La and Pr in zircon, we prefer a calibration based on these two elements to calculate Ce*. In part, this is because chemical fractionation is more likely to affect La → Pr in a generally similar manner, when compared to Ce and Sm; e.g., evidence for fractionation of the LREE from Sm is seen in Fig. 12. In addition, there is an internal check for the Ce anomaly-based calibration that is anchored by a simple theoretical prediction: if zircon $Ce_{CN}/\sqrt{(La_{CN} \times Pr_{CN})} < 1$, the system has violated the assumptions, and that analysis cannot be used to infer oxidation state. We rely on this to exclude some natural measurements from consideration (section 4.4).

5.3. *The role of experimental fluid composition and the effect on anomalies in zircon*

The fluid composition could influence the speciation of Eu and Ce in the fluid, the partition coefficients, and calculated redox anomalies for both elements. We can explore this by comparing the anomalies at a

given fo_2 and temperature vs. fluid composition dictated by mix 1 and mix 2. As noted, mix 1 does not contain NaCl whereas mix 2 has ~15 wt % NaCl, represented as a percentage of the total mass of the solids plus fluids at the start of an experiment. We also evaluate the variable fluid

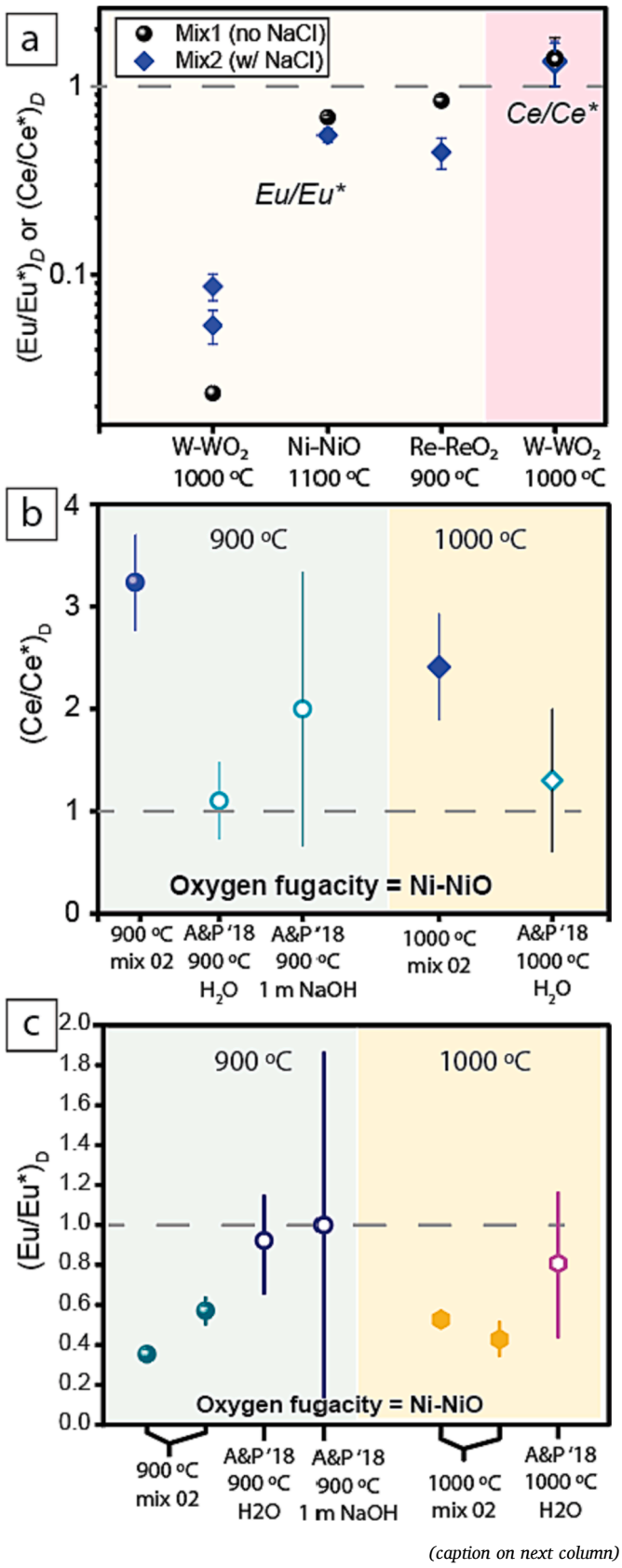

(caption on next column)

Fig. 13. (a) In the experiments conducted with two different mix compositions (refer to Table 1), the zircon Eu anomalies reveal how the composition of the fluid affects the anomaly, for a given T and fo_2. For zircon Ce anomalies, a "mix 1" experiment (zfl-1000-W-MIX1) compared to two "mix 2" experiment products (13-1000-Wm2 & 32-1000-Wm2) show no resolvable difference. (b,c) We compare anomalies from our experiments to those produced by Ayers and Peters (2018) at the same T and fo_2. Once errors are considered, the apparent effect of fluid composition is not obvious though Ayers and Peters (2018) conducted experiments under different protocols; e.g., they used seed crystals (vs. unseeded mineral synthesis done here). Ayers and Peters (2018) then analyzed partially reacted zircons and employed mass balance calculations to derive Ce/Eu anomalies in place of direct ICP-MS measurements of the experimental fluids.

compositions presented in Ayers and Peters (2018). Our experimental results confirm a fluid compositional control on the intensity for Eu anomalies (Fig. 13**a**). On the other hand, zfl-1000-W-MIX1 (mix 1, no NaCl added) vs. 13-1000-Wm2 & 32-1000-Wm2 (mix 2, both with NaCl) show no resolvable differences in the Ce anomalies. When comparing the data from Ayers and Peters (2018) to ours, no significant differences in the anomalies are obvious, after accounting for errors (Fig. 13**b, c**). The current data allow for only a basic evaluation of the fluid composition effect, and this limitation should be kept in mind when using the calibrations provided here to measure oxygen fugacity. However, we still regard the salinity of mix 2 as a broadly suitable proxy of natural systems.

To reinforce this, in ~10 magmatic systems with associated hydrothermal fluids, it was discovered that these fluids typically exhibit salinities that range from 2 to 13 wt% NaCl equivalent, averaging around 5 wt% NaCl equivalent (Audétat et al., 2008). The same study also reported instances of magmatic systems containing brines with the NaCl equivalent surpassing 26 wt%, a concentration indicative of NaCl saturation at room temperature. In a separate compilation study, data collected on formation waters and metamorphic fluids, whether sampled during drilling or preserved in fluid inclusions, suggest that ~75 % of the investigated fluids have a salinity that varies from 1 to approximately 30 wt% NaCl equivalent (Yardley and Graham, 2002). These two compilation studies – one centered on hydrothermal fluids connected to magmatic systems, the other focused on fluids associated with metamorphism – underscore the significant salinity fluctuation in high-temperature lithospheric fluids. However, the "mix 2" set of experiments better encapsulates the expected salinity for natural high-temperature crustal fluids, compared to the "mix 1" experiment where NaCl was absent.

5.4. Application of the experimental results

With the abovementioned considerations and assumptions in place, which should be kept in mind here, we apply the experimental calibrations to natural hydrothermal zircon-bearing localities. For all cases, the oxygen fugacity is calculated using with and we have also substituting Eq. (14a) into Eq. (5b). In general, we explore samples with REE and Ti in zircon analyses, as a T calculation is required to calculate the oxygen fugacity. Unless otherwise noted, T is calculated with the Ti-in-zircon thermometer assuming unity SiO_2 and TiO_2 activities (Ferry and Watson, 2007). Oxygen fugacity values are reported relative to the FMQ equilibrium (O'Neill, 1987), and errors are reported as the standard deviation of each individual dataset. Recall that fluid precipitated zircons can have high porosity and sponge-like textures, where analyses of these grains are more likely to capture fluid or mineral inclusions in the analyte. Such analyses are subject to sources of error in the chemical quantification that could propagate an error in the fo_2 calculation. Thus, for each dataset discussed, we note the analytical method employed by the authors for the zircon measurements (either SIMS – secondary ion mass spectrometry or LA-ICP-MS). The latter method samples a much larger volume and is therefore more susceptible to contamination via

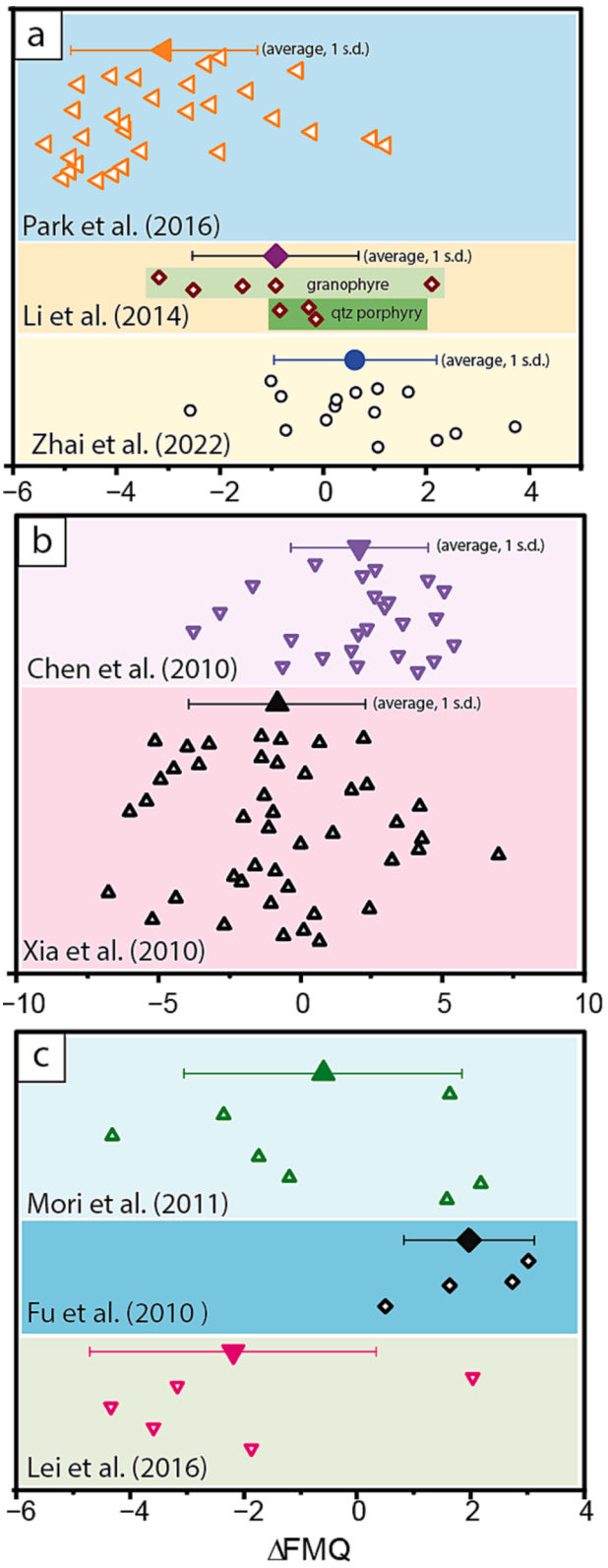

Fig. 14. Oxygen fugacity calculations produced from subsolidus zircon chemistry. Individual measurements are shown in open symbols, closed symbols represent the averages and standard deviations of the datasets. (a) Oxygen fugacity calculations from different hydrothermal ore deposits; see section 5.4.1. (b) Oxygen fugacity calculations of deep crustal fluids produced from the Dabie Sulu orogeny; see section 5.4.2. (c) Oxygen fugacity calculations from three different jadeitites; see section 5.4.3.

fluid/mineral inclusions, or metamict grain regions.

5.4.1. *Oxygen fugacity of hydrothermal ore deposits*

Accessory minerals, like zircon are frequently associated with hydrothermal ore deposits. In this context they offer an opportunity to determine the age of mineralization, and along with our calibration, the oxidation state of the fluid. The latter is a key variable that can control the stability and deposition of key minerals in ore reposits. Some zircons in these systems reflect magmatic chemistry, which is not considered here; we present oxygen fugacity calculations for zircon regions that are consistent with hydrothermal crystallization only.

Zhai et al. (2022) investigated the Ikalamavony Group rocks in Madagascar, which include migmatite gneiss, paragneiss, quartzite, and marble. Faults and cracks in these rocks contain zircon bearing hydrothermal veins. The veins were interpreted to have been produced by the metamorphic release of volatile components from Zr-rich sedimentary rocks; outside of Hf and Zr there is no evidence for mineralization. Using the LA-ICP-MS data for this study yields and average fo_2 of FMQ+0.6 ± 1.6 (Fig. 14a).

In a separate study, Li et al. (2014) reported LA-ICP-MS data for zircons from the Huangshaping polymetallic deposit, located in the central Nanling region of South China. Different types of mineralization are attributed to the quartz porphyry, granophyre, and granite porphyry granitoids. Zircon alteration is interpreted to be the result of hydrothermal fluid activity associated with the mineralization events. Only zircon domains identified as “hydrothermal” by the authors are considered in this analysis. Zircon U–Pb geochronology indicates mineralization at approximately 190 Ma, with Cu-Pb-Zn mineralization associated with the quartz porphyry and granophyre. We calculate the oxygen fugacity values for this mineralization event for the quartz porphyry (FMQ-0.4 ± 0.4; n = 3) and granophyre (FMQ-1.2 ± 2.2; n = 5). The small number of analyses does not permit a robust assessment of whether there is a statistical difference in oxygen fugacity between the two systems, which together yield an average fo_2 value of FMQ-0.9 ± 1.6 (Fig. 14a). The authors suggest that the early stage of mineralization likely involved a single, relatively cool, reduced, and rapidly ascending fluid. This interpretation is broadly consistent with calculations which indicate the fluid was not oxidized.

The Weondong region, South Korea has potential for mineralization of Pb–Zn–W and Zr–REE–Nb. Park et al. (2016) analyzed zircon from leucocratic granite by SIMS. Following the initial formation of primary zircon during the late magmatic phase, the zircon crystals show evidence of secondary internal recrystallization, which supports the presence post-magmatic fluids at ~50 Ma. Post-magmatic fluids, rich in F, transported Zr resulting in the characteristic overgrowths observed on magmatic zircon. In the only case like this that we present here, we estimate the oxygen fugacity by assuming a temperature not intrinsic to the zircon; that is, no Ti contents in zircon were reported by Park et al. (2016). Assuming a crystallization temperature of 550 °C yields an oxygen fugacity of FMQ-3.1 ± 1.8 (Fig. 14a). While the predicted fo_2 of the fluid is reduced, it also carries with it the largest uncertainty in the absence of a more direct T constraint. If the crystallization T was 500 or 600 °C (vs. 550 °C), the average calculated fluid fo_2 would be FMQ-4.2 or FMQ-2.1, respectively. The Eu anomalies for these zircons are very low with an average value of 0.002 ± 0.001, which is constant with reducing conditions.

5.4.2. *Oxygen fugacity of fluids during Dabie-Sulu orogenesis*

The Dabi-Sulu orogenic belt formed during the continent–continent collision between the North and South China blocks during the Triassic under low-T/ultrahigh pressure conditions (~700 °C and ~3 GPa; Xia et al., 2008). Xia et al. (2010) provide geochemical evidence for the existence of supercritical fluid interactions that produced zircon, and zircon chemistry has been used to investigate the properties of metamorphic fluid during the collision (Xia et al., 2010; Chen et al., 2010). We use zircon data from Xia et al. (2010) which give an oxygen fugacity

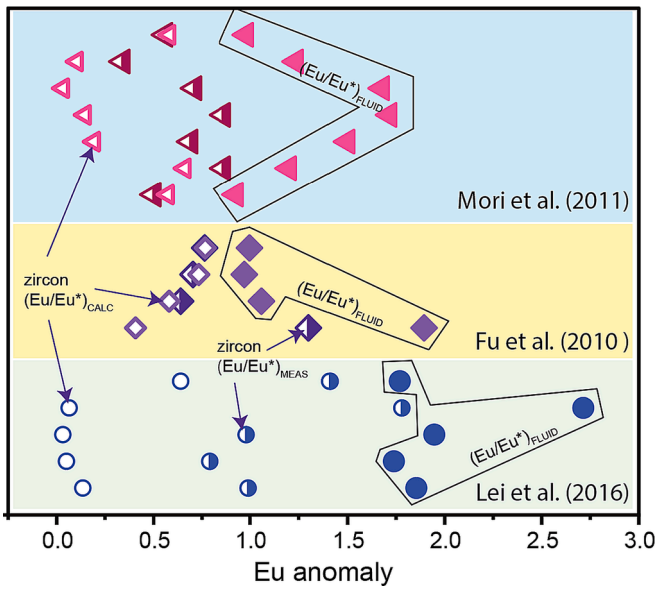

Fig. 15. Measured zircon Eu anomalies (open symbols), calculated zircon Eu anomalies (half symbols), and calculated Eu anomalies of the fluid during zircon crystallization (closed symbols). To get the fluid Eu anomalies, the method involves calculating the fo_2 with the Ce anomaly calibration and then using that to calculate the expected Eu anomaly for the zircon. This is compared to the measured value, and the offset between calculated and measured is used to derive the fluid Eu anomaly, which ranges between 1 and 3. We assume no compositional control on the Eu anomalies as a function of fluid composition (but see Fig. 13 and associated discussion).

of FMQ-0.8 ± 3.1 whereas the results from Chen et al. (2010) yield an fo_2 of FMQ + 2.1 ± 2.4 (Fig. 14b). Note that for Xia et al. (2010) 21 out of 66 analyzes had Ce anomalies < 1, meaning the oxygen fugacity could not be calculated as a defined value. Despite the large error, the datasets from these two studies are distinguishable. Specifically, an independent two-sample *t*-test yields a p-value of ~0.00006, indicating a statistically significant difference between the groups (n = 25 for Chen et al., 2010; n = 45 for Xia et al., 2010). Because the data are sub-normally distributed, we also ran a Mann-Whitney *U* test, which indicates a significant difference in the distributions of the two datasets as well. Xia et al. (2010) samples were collected more than 100 km south of those reported in Chen et al. (2010), and thus indicate a fluid with a heterogeneous oxidation state during the orogeny.

5.4.3. *Oxygen fugacity of fluids interacting with jadeitite*

Jadeitites are produced by hydrothermal fluids during high-pressure metamorphism in subduction zones. They are thought to form in ultramafic rocks within the subduction channel, likely originating from the mantle wedge (Flores et al., 2013; Harlow et al., 2015). Consequently, zircons extracted from these rocks could offer valuable information about the oxidation state of fluids in the mantle wedge. This constraint could serve a vital role to better understand the redox evolution within subduction zones. For example, while we have a general understanding of the redox conditions of volcanic outputs such as arc basalts (e.g., Mallmann and O'Neill, 2009; Kelly and Cottrell, 2009), as well as some insights into inputs like global subducting sediments (Plank and Langmuir, 1998), another potential key component, deep fluids, remains less constrained.

We explore zircon samples recorded from these rocks from different localities and compare the fluid oxidation state during hydrothermal alteration. Lei et al. (2016) analyzed zircon by LA-ICP-MS from jadeitite located in the northern part of the Sagaing fault belt in Myanmar, and noted that only a small fraction of the analyses (5 out of 26) were interpreted to be a recorder of high temperature fluid whereas the rest were considered to be inherited (igneous) grains. We calculate the fo_2 of the fluid via hydrothermal zircon analyses (n = 5) that formed within the subduction zone to get an average value of FMQ-2.2 ± 2.5 (Fig. 14c). Fu et al. (2010) quantified trace element chemistry by LA-ICP-MS for zircon found in jadeitite for a serpentinite mélange from Osayama, SW Japan. The LA-ICP-MS measurements were performed on clear areas of zircon, though the authors note that microinclusions may have been inadvertently included in the analyses, owing to the comparatively large diameter (30 μm) of the laser spot. Analyses were also classified according to zircon formation conditions; using zircon analyses that represent hydrothermal conditions we calculate an oxygen fugacity of FMQ + 2 ± 1.1 (Fig. 14c). Mori et al. (2011) conducted a study on jadeitite from the Nishisonogi metamorphic rocks in Kyushu, Japan. They focused on examining the chemistry rims of grains around inherited cores by LA-ICP-MS. They interpret the grain rims to have precipitated from aqueous fluids during the formation of jadeitite. Application of our calibration to these rims yields an fo_2 of FMQ-0.6 ± 2.5 (Fig. 14c).

Fluid precipitated zircons found in jadeitites have only slightly negative (or in some cases positive) Eu anomalies. Jadeitite *whole rocks* generally have positive Eu anomalies (Morishita et al., 2007; Shi et al., 2008; Yui et al., 2010,2012), which has been attributed to plagioclase breakdown during fluid-rock interaction (e.g., Yui et al., 2010). Because plagioclase has a positive Eu anomaly – due to the highly compatible nature of Eu^{2+} relative to the trivalent REEs – its breakdown will yield a fluid that also has a positive Eu anomaly. We can calculate the Eu anomaly of the fluid by substituting in the calculated oxygen fugacity into Eq. (13), and then solving for the Eu anomaly zircon at that oxygen fugacity ($(Eu/Eu^*)_{CALC}$; Fig. 15).

Note that this calculation assumes that the maximum possible Eu anomaly is 1. Now, this value can be compared to the *measured* Eu anomaly ($(Eu/Eu^*)_{MEAS}$; Fig. 15), and the difference between these two values is the "excess" in the Eu anomaly above 1. We can the calculate the Eu anomaly of the fluid ($(Eu/Eu^*)_{FLUID}$; Fig. 15). The $(Eu/Eu^*)_{FLUID}$ values range from ~ 1 to almost 3, which supports the interpretation that plagioclase (or another mineral with positive Eu anomalies) underwent breakdown contemporaneously with zircon crystallization from the fluid.

6. Conclusions

Quantifying the oxygen fugacity of lithospheric fluids is a difficult task. The experiments presented herein show a systematic behavior between Ce and Eu anomalies in zircon and the oxygen fugacity of the corresponding fluid. Besides oxygen fugacity, Ce anomalies also exhibit sensitivity to temperature necessitating some other temperature-based crystallization constraint. In contrast, there is lack of a systematic 1/T trend for zircon Eu anomalies. We use these first order observations to fit the data to functions that derive the change in Ce/Eu anomalies as a function of oxygen fugacity, and T in the case of Ce anomalies. We find that Ce and Eu anomalies which are fit using the calculated anomalies from the bracketing REEs rather than those obtained via the lattice strain model provide the most robust fit to the data.

Even though Ce anomalies in zircon depend on T, we propose that this will be simplest and most broadly applicable fo_2 calibration. However, this quantification does rely on the absence of (or limited) inheritance of a Ce anomaly in hydrothermal fluid precipitating zircon. Conversely, situations where a fluid exhibits an Eu anomaly – either positive or negative – are likely to be quite common, which means that the magnitude of the Eu anomaly in zircon should be considered to be a combination of multiple processes. This includes crystallization of other major rock-forming minerals – e.g, feldspar and pyroxene – and oxygen fugacity. If the REE content of fluid can be directly measured from a coexisting fluid inclusion and reasonably assumed to be in equilibrium with zircon, these anomalies could be compared for agreement, as schematically shown on the redox concordia diagram.

We also demonstrate that zircon Eu anomalies are partially influenced by the fluid composition, in addition to oxygen fugacity. While the Eu anomaly calibration represented by Eq. (13) could be used to estimate the Eu anomaly of the fluid with an independent fo_2 constraint, the dependence on the fluid composition effect should be considered (e.g., vs. fluid salinity along with other volatile components). The same could also be true for Ce anomalies in zircon, as the current experimental dataset on this topic is limited.

With the above caveats and assumptions noted, we apply our results to yield fo_2 calibrations on shallow (<5 kbar) hydrothermal systems, which are also of interest for critical mineral research, because oxygen fugacity influences mineralization potential (Candela, 1992; Blevin and Chappell, 2011; Yardley and Bodnar, 2014). We also apply our calibration to subduction zone systems, in which fluid precipitated zircon, in the Dabie Sulu orogen, and show that the oxidation state of this fluid is heterogenous. We note however that in some cases, Ce anomalies were < 1 and therefore no meaningful fo_2 value can be derived.

In addition, fluid precipitated zircon jadeitites were used to calculate the oxygen fugacity values Sagaing fault belt in Myanmar, Osayama serpentinite mélange, Japan, and Nishisonogi metamorphic rocks in Kyushu, Japan. While there are hints of fo_2 differences among these different settings, the number of analyses from each location (~5) and the distribution of the data do not permit a stronger statement. We were also able to use the available data to calculate the expected Eu anomaly of the fluid. With this information, we conclude that the zircons in jadeitites formed in the presence of a fluid with a positive Eu anomaly, probably due to plagioclase decomposition. Based on our experiments and analyses, we demonstrate that zircon Ce and Eu anomalies can be effectively utilized as proxies for determining the oxygen fugacity of high-temperature lithospheric fluids. These findings not only enhance our understanding of fluid-mineral interactions in critical element-bearing systems but also provide valuable insights into the oxygen fugacity conditions during plate boundary processes.

Data availability

Data are available through Mendeley Data at https://doi.org/10.17632/y9bzvzctwb.2.

CRediT authorship contribution statement

Dustin Trail: Conceptualization, Formal analysis, Funding acquisition, Investigation, Methodology, Resources, Supervision, Visualization, Writing – original draft. **Wriju Chowdhury:** Data curation, Formal analysis, Investigation, Methodology, Validation, Writing – review & editing. **Nicholas D. Tailby:** Formal analysis, Investigation, Methodology, Writing – review & editing. **Michael R. Ackerson:** Investigation, Writing – review & editing.

Declaration of competing interest

The authors declare that they have no known competing financial interests or personal relationships that could have appeared to influence the work reported in this paper.

Acknowledgements

This research was supported by NSF EAR-175190, EAR-2240755, and NASA grant 80NSSC19M0069. Yanling Wang, Jacob Buettner, Kyrsten Johnston, and Hsin-Yu Chen are thanked for technical assistance. We thank John C. Ayers, Brenhin Keller, and an anonymous reviewer whose comments helped improve the quality of the manuscript.

Appendix A. Supplementary material

Supplementary material to this article can be found online at https://doi.org/10.1016/j.gca.2024.01.024.

References

Aranovich, L.Y., Makhluf, A.R., Manning, C.E., Newton, R.C., 2014. Dehydration melting and the relationship between granites and granulites. Precamb. Res. 253, 26–37.
Audétat, A., 2019. The metal content of magmatic-hydrothermal fluids and its relationship to mineralization potential. Economic Geol. 114, 1033–1056.
Ayers, J.C., Peters, T.J., 2018. Zircon/fluid trace element partition coefficients measured by recrystallization of Mud Tank zircon at 1.5 Pa and 800–1000 °C. Geochim. Cosmochim. Acta 223, 60–74.
Baxter, E.F., Caddick, M.J., 2013. Garnet growth as a proxy for progressive subduction zone dehydration. Geology 41, 643–646.
Bell, E.A., Boehnke, P., Harrison, T., 2016. Recovering the primary geochemistry of Jack Hills zircons through quantitative estimates of chemical alteration. Geochimica Et Cosmochimica Acta 191, 187–202.
Berry, A.J., Danyushevsky, L.V., O'Neill, H., St, C., Newville, M., Sutton, S.R., 2008. Oxidation state of iron in komatiitic melt inclusions indicates hot Archaean mantle. Nature 455, 960–963.
Blevin, P.L., 2004. Redox and compositional parameters for interpreting the granitoid metallogeny of Eastern Australia: Implications for gold-rich ore systems. Resour. Geol. 54 (3), 241–252.
Blevin, P.L., Chappell, B.W., 2011. The role of magma sources, oxidation states and fractionation in determining the granite metallogeny of eastern Australia. Earth Environ. Sci. Trans. Royal Soc. Ed. 83, 305–316.
Blundy, J., Wood, B., 2003. Partitioning of trace elements between crystals and melts. Earth Planet. Sci. Lett. 210, 383–397.
Bucholz, C.E., Kelemen, P.B., 2019. Oxygen fugacity at the base of the Talkeetna arc, Alaska. Contrib. Mineral. Petrol. 174.
Burnham, A.D., Berry, A.J., 2012. An experimental study of trace element partitioning between zircon and melt as a function of oxygen fugacity. Geochim. Cosmochim. Acta 95, 196–212.
Candela, P.A., 1992. Controls on ore metal ratios in granite-related ore systems: an experimental and computational approach. Earth Environ. Sci. Trans. Royal Soc. Ed. 83, 317–326.
Canil, D., 2002. Vanadium in peridotites mantle redox and tectonic environments archean to present. Earth Planet. Sci. Lett. 195, 75–90.
Carmichael, I.S.E., 1991. The redox states of basic and silicic magmas: a reflection of their source regions? Contrib. Mineral. Petrol. 106, 129–141.
Chen, R.-X., Zheng, Y.-F., Xie, L., 2010. Metamorphic growth and recrystallization of zircon: Distinction by simultaneous in-situ analyses of trace elements, U–Th–Pb and Lu–Hf isotopes in zircons from eclogite-facies rocks in the Sulu orogen. Lithos 114 (1–2), 132–154.
Chowdhury, W., Trail, D., Bell, E.A., 2020. Boron partitioning between zircon and melt: insights into Hadean, modern arc, and pegmatitic settings. Chem. Geol. 551.
Chowdhury, W., Trail, D., Miller, M., Savage, P.S., 2023. Eoarchean and Hadean melts reveal arc-like trace element and isotopic signatures. Nat Commun 14, 1140.
Colman, D.R., Lindsay, M.R., Boyd, E.S., 2019. Mixing of meteoric and geothermal fluids supports hyperdiverse chemosynthetic hydrothermal communities. Nat. Commun. 10, 1–13.
Cottrell, E., Birner S.K., Brounce, M., Davis, F.A., Waters, L.E., Kelley, K.A. 2021. Oxygen fugacity across tectonic settings. In: Magma Redox Geochemistry, pp. 33-61.
Cottrell, E., Kelley, K.A., 2011. The oxidation state of Fe in MORB glasses and the oxygen fugacity of the upper mantle. Earth Planet. Sci. Lett. 305, 270–282.
de Hoog, J.C.M., Lissenberg, C.J., Brooker, R.A., Hinton, R., Trail, D., Hellebrand, E., 2014. Hydrogen incorporation and charge balance in natural zircon. Geochim. Cosmochim. Acta 141, 472–486.
Delano, J.W., 2001. Redox history of the Earth's interior since ~3900 Ma: implications for prebiotic molecules. Origins Life Evolut. Biosphere 31, 311–341.
Drake, M.J., Weill, D., 1975. Partition of Sr, Ba, Ca, Y, Eu^{2+}, Eu, and other REE between plagioclase feldspar and magmatic liquid: an experimental study. Geochim. Cosmochim. Acta 39, 689–712.
Ferry, J.M., Watson, E.B., 2007. New thermodynamic models and revised calibrations for the Ti-in-zircon and Zr-in-rutile thermometers. Contrib. Mineral. Petrol. 154, 429–437.
Fu, B., Mernagh, T.P., Kita, N.T., Kemp, A.I.S., Valley, J.W., 2009. Distinguishing magmatic zircon from hydrothermal zircon: a case study from the Gidginbung high-sulphidation Au–Ag–(Cu) deposit, SE Australia. Chem. Geol. 259, 131–142.
Fu, B., Valley, J.W., Kita, N.T., Spicuzza, M.J., Paton, C., Tsujimori, T., Bröcker, M., Harlow, G.E., 2010. Multiple origins of zircons in jadeitite. Contrib. Mineral. Petrol. 159 (6), 769–780.
Gao, L., Liu, S., Cawood, P.A., Hu, F., Wang, J., Sun, G., Hu, Y., 2022. Oxidation of Archean upper mantle caused by crustal recycling. Nat Commun 13, 3283.
Ghiorso, M.S., Evans, B.W., 2008. Thermodynamics of rhombohedral oxide solid solutions and a revision of the Fe-Ti two-oxide geothermometer and oxygen-barometer. Am. J. Sci. 308 (9), 957–1039.
Ghiorso, M.S., Gualda, G.A.R., 2013. A method for estimating the activity of titania in magmatic liquids from the compositions of coexisting rhombohedral and cubic iron–titanium oxides. Contrib. Mineral. Petrol. 165, 73–81.

Hacker, B.R., Peacock, S.M., Abers, G.A., Holloway, S.D., 2003. Subduction factory 2. Are intermediate-depth earthquakes in subducting slabs linked to metamorphic dehydration reactions? J. Geophys. Res. 108, 11-11–11-18.
Hanchar, J.M., Finch, R.J., Hoskin, P.W.O., Watson, E.B., Cherniak, D.J., Mariano, A.N., 2001. Rare earth elements in synthetic zircon: Part 1. Synthesis, and rare earth element and phosphorus doping. Am. Mineral. 86, 667–680.
Harley, S.L., Kelly, N.M., Möller, A., 2017. Zircon behaviour and the thermal histories of mountain chains. Elements 3, 25–30.
Harlow, G.E., Tsujimori, T., Sorensen, S.S., 2015. Jadeitites and Plate Tectonics. Ann. Rev. Earth Planetary Sci. 43 (1), 105–138.
Hildreth, W., Wilson, C.J.N., 2007. Compositional zoning of the Bishop Tuff. J. Petrol. 48, 951–999.
Hirschmann, M.M., 2012. Magma ocean influence on early atmosphere mass and composition. Earth Planet. Sci. Lett. 341–344, 48–57.
Holycross, M.E., Cottrell, E., 2022. Experimental quantification of vanadium partitioning between eclogitic minerals (garnet, clinopyroxene, rutile) and silicate melt as a function of temperature and oxygen fugacity. Contrib. Mineral Petrol. 177.
Holycross, M.E., Cottrell, E., 2023. Garnet crystallization does not drive oxidation at arcs. Science 380, 506–509.
Hoskin, P.W.O., 2005. Trace-element composition of hydrothermal zircon and the alteration of Hadean zircon from the Jack Hills. Australia. Geochim. Cosmochim. Acta 69, 637–648.
Hoskin, P.W.O., Black, L.P., 2000. Metamorphic zircon formation by solid-state recrystallization of protolith igneous zircon. J. Metamorph. Geol. 18, 423–439.
Jiang, W.-C., Li, H., Evans, N.J., Wu, J.-H., 2019. Zircon records multiple magmatic-hydrothermal processes at the giant Shizhuyuan W–Sn–Mo–Bi polymetallic deposit, South China. Ore Geol. Rev. 115.
Karner, J.M., Papike, J.J., Sutton, S.R., Burger, P.V., Shearer, C.K., Le, L., Newville, M., Choi, Y., 2010. Partitioning of Eu between augite and a highly spiked martian basalt composition as a function of oxygen fugacity (IW-1 to QFM): Determination of Eu^{2+}/Eu^{3+} ratios by XANES. American Mineralogist 95, 410–413.
Kelly, K.A., Cottrell, E., 2009. The oxidation state of subduction zome magmas. Science 325, 605–607.
Lei, W., Shi, G., Santosh, M., Ng, Y., Liu, Y., Wang, J., Xie, G., Ju, Y., 2016. Trace element features of hydrothermal and inherited igneous zircon grains in mantle wedge environment: A case study from the Myanmar jadeitite. Lithos 266–267, 16–27.
Li, J., Cao, S., Cheng, X., Jin, L., Lyu, M., 2023. Magmatic-hydrothermal evolution and tectonic implications of granitic pegmatites from the Ailao Shan-Red River shear zone in Southeast Asia. Lithos 442–443.
Li, C., Li, L., Li, S.-R., Santosh, M., Shen, J.-F., 2022. Geochemistry of hydrothermal zircon as a proxy to fingerprint ore fluids in late Mesozoic decratonic gold deposits. Ore Geol. Rev. 143.
Li, J.-X., Qin, K.-Z., Li, G.-M., Evans, N.J., Zhao, J.-X., Yue, Y.-H., Xie, J., 2018. Volatile variations in magmas related to porphyry Cu-Au deposits: Insights from amphibole geochemistry, Duolong district, central Tibet. Ore Geol. Rev. 95, 649–662.
Li, H., Watanabe, K., Yonezu, K., 2014. Zircon morphology, geochronology and trace element geochemistry of the granites from the Huangshaping polymetallic deposit, South China: implications for the magmatic evolution and mineralization processes. Ore Geol. Rev. 60, 14–35.
Liang, Y., Sun, C., Yao, L., 2013. A REE-in-two-pyroxene thermometer for mafic and ultramafic rocks. Geochim. Cosmochim. Acta 102, 246–260.
Mallmann, G., O'Neill, H.S.C., 2009. The Crystal/Melt Partitioning of V during Mantle Melting as a Function of Oxygen Fugacity Compared with some other Elements (Al, P, Ca, Sc, Ti, Cr, Fe, Ga, Y, Zr and Nb). J. Petrol. 50, 1765–1794.
Manning, C.E., Mojzsis, S.J., Harrison, T.M., 2006. Geology, Age and Origin of Supracrustal Rocks at Akilia, West Greenland. Am. J. Sci. 306, 303–366.
McCollom, T.M., Shock, E.L., 1998. Fluid-rock interactions in the lower oceanic crust: thermodynamic models of hydrothermal alteration. J. Geophys. Res.: Solid Earth 103, 547–575.
Mills, R.A., Wells, D.M., Roberts, S., 2001. Genesis of ferromanganese crusts from the TAG hydrothermal field. Chem. Geol. 176, 283–293.
Möller, V., Williams-Jones, A.E., 2017. Magmatic and Hydrothermal Controls on the Mineralogy of the Basal Zone, Nechalacho REE-Nb-Zr Deposit, Canada. Econ. Geol. 112, 1823–1856.
Mori, Y., Orihashi, Y., Miyamoto, T., Shimada, K., Shigeno, M., Nishiyama, T., 2011. Origin of zircon in jadeitite from the Nishisonogi metamorphic rocks, Kyushu, Japan. J. Metamorph. Geol. 29 (6), 673–684.
Morishita, T., Arai, S., Ishida, Y., 2007. Trace element compositions of jadeite (+ omphacite) in jadeitites from the Itoigawa-Ohmi district, Japan: implications for fluid processes in subduction zones. Island Arc 16 (1), 40–56.
Muth, M.J., Cottrell, E., 2023. No detectable redox exchange between sulfur and iron during rapid cooling of basalts. Earth Planet. Sci. Lett. 616, 118210.
Nazari-Dehkordi, T., Robb, L., 2022. Zircon mineral chemistry and implications for magmatic-hydrothermal evolution of the granite-hosted Zaaiplaats Sn deposit, Bushveld Large Igneous Province. South Africa. Lithos 416–417.
O'Neill, H.S.C., 1987. Quartz-fayalite-iron and quartz-fayalite-magnetite equilibria and the free energy of formation of fayalite (Fe_2SiO_4) and magnetite (Fe_3O_4). Am. Mineral. 72 (1–2), 67–75.
O'Neill, H.S.C., Nell, J., 1997. Gibbs free energies of formation of RuO_2, lrO_2, and OsO_2: a high-temperature electrochemical and calorimetric study. Geochim. Cosmochim. Acta 61, 5279–5293.
O'Neill, H.S.C., Pownceby, M.I., 1993. Thermodynamic data from redox reactions at high temperatures. I. An experimental and theoretical assessment of the electrochemical method using stabilized zirconia electrolytes, with revised values for the Fe - "FeO", Co- CoO, Ni - NiO and Cu- CuzO oxygen buffers, and new data for the W-WO_2 buffer. Contrib. Mineral. Petrol. 114, 296–314.
Park, C., Song, Y., Chung, D., Kang, I.-M., Khulganakhuu, C., Yi, K., 2016. Recrystallization and hydrothermal growth of high U–Th zircon in the Weondong deposit, Korea: Record of post-magmatic alteration. Lithos 260, 268–285.
Paton, C., Hellstrom, J., Paul, B., Woodhead, J., Hergt, J., 2011. Iolite: freeware for the visualisation and processing of mass spectrometric data. J. Analytical Atomic Spectrometry 26.
Pelleter, E., Cheilletz, A., Gasquet, D., Mouttaqi, A., Annich, M., El Hakour, A., Deloule, E., Féraud, G., 2007. Hydrothermal zircons: A tool for ion microprobe U–Pb dating of gold mineralization (Tamlalt–Menhouhou gold deposit — Morocco). Chem. Geol. 245, 135–161.
Pettke, T., Audétat, A., Schaltegger, U., Heinrich, C.A., 2005. Magmatic-to-hydrothermal crystallization in the W–Sn mineralized Mole Granite (NSW, Australia). Chem. Geol. 220, 191–213.
Plank, T., Langmuir, C.H., 1998. The chemical composition of subducting sediment and its consequences for the crust and mantle. Chem. Geol. 145, 325–394.
Pownceby, M.I., O'Neill, H.S.C., 1994. Thermodynamic data from redox reactions at high temperatures. IV. Calibration of the Re-ReOz oxygen buffer from EMF and NiO + Ni-Pd redox sensor measurements. Contrib. Mineral. Petrol. 118, 130–137.
Rancourt, D.G., Fortin, D., Pichler, T., Thibault, P.-J., Lamarche, G., Morris, R.V., Mercier, P.H.J., 2001. Mineralogy of a natural As-rich hydrous ferric oxide coprecipitate formed by mixing of hydrothermal fluid and seawater: Implications regarding surface complexation and color banding in ferrihydrite deposits. Am. Mineral. 86, 834–851.
Reid, M.R., Vazquez, J.A., Schmitt, A.K., 2010. Zircon-scale insights into the history of a Supervolcano, Bishop Tuff, Long Valley, California, with implications for the Ti-in-zircon geothermometer. Contrib. Mineral. Petrol. 161, 293–311.
Rubatto, D., 2017. Zircon: the metamorphic mineral. Rev. Mineral. Geochem. 83, 261–295.
Rubatto, D., Regis, D., Hermann, J., Boston, K., Engi, M., Beltrando, M., McAlpine, S.R.B., 2011. Yo-yo subduction recorded by accessory minerals in the Italian Western Alps. Nat. Geosci. 4, 338–342.
Rudnick, R.L., Gao, S., 2003. Composition of the continental crust. Treatise Geochem. 3, 1–64.
Schaltegger, U., Pettke, T., Audétat, A., Reusser, E., Heinrich, C.A., 2005. Magmatic-to-hydrothermal crystallization in the W–Sn mineralized Mole Granite (NSW, Australia). Chem. Geol. 220, 215–235.
Schlüter, J., Malcherek, T., Husdal, T.A., 2009. The new mineral stetindite, $CeSiO_4$, a cerium end-member of the zircon group. Neues Jahrbuch Für Mineralogie-Abhandlungen: J. Mineral. Geochem. 186, 195–200.
Schmidt, C., Gottschalk, M., Zhang, R., Lu, J., 2021. Oxygen fugacity during tin ore deposition from primary fluid inclusions in cassiterite. Ore Geol. Rev. 139, 1–5.
Schmitt, A.K., 2011. Uranium series accessory crystal dating of magmatic processes. Annu. Rev. Earth Planet. Sci. 39, 321–349.
Schoene, B., 2014. U–Th–Pb Geochronology. Treatise Geochem. 4, 341–378.
Shannon, R.T., 1976. Revised effective ionic radii and systematic studies of interatomic distances in halides and chalcogenides. Acta Crystallographica Section A: Crystal Phys. Diffraction Theor. General Crystallogr. 32, 751–767.
Shearer, C.K., Papike, J.J., Karner, J.M., 2006. Pyroxene europium valence oxybarometer: effects of pyroxene composition, melt composition, and crystallization kinetics. Am. Mineral. 91, 1565–1573.
Shi, G., Cui, W., Cao, S., Jiang, N., Jian, P., Liu, D., Miao, L., Chu, B., 2008. Ion microprobe zircon U–Pb age and geochemistry of the Myanmar jadeitite. J. Geol. Soc. London 165, 221–234.
Soman, A., Geisler, T., Tomaschek, F., Grange, M., Berndt, J., 2010. Alteration of crystalline zircon solid solutions: a case study on zircon from an alkaline pegmatite from Zomba–Malosa, Malawi. Contrib. Mineral. Petrol. 160, 909–930.
Sossi, P.A., Burnham, A.D., Badro, J., Lanzirotti, A., Newville, M., O'Neill, H.S.C., 2020. Redox state of Earth's magma ocean and its Venus-like early atmosphere. Sci. Adv. 6, eabd1387.
Sun, S.-S., McDonough, W.F., 1989. Chemical and isotopic systematics of oceanic basalts: implications for mantle composition and processes. Geol. Soc. London Special Publications 42 (1), 313–345.
Tailby, N.D., Trail, D., Watson, E.B., Lanzirotti, A., Newville, M., Wang, Y., 2023. Eu speciation in apatite at 1 bar: an experimental study of valence-state partitioning by XANES, lattice strain and Eu/Eu* in basaltic systems. Am. Mineral. 108, 789–813.
Thomas, J., Bodnar, R., Shimizu, N., Sinha, A., 2002. Determination of zircon/melt trace element partition coefficients from SIMS analysis of melt inclusions in zircon. Geochim. Cosmochim. Acta 66, 2887–2901.
Toscano, M., Pascual, E., Nesbitt, R.W., Almodóvar, G.R., Sáez, R., Donaire, T., 2014. Geochemical discrimination of hydrothermal and igneous zircon in the Iberian Pyrite Belt, Spain. Ore Geol. Rev. 56, 301–311.
Trail, D., 2018. Redox-controlled dissolution of monazite in fluids and implications for phase stability in the lithosphere. Am. Mineral. 103, 453–461.
Trail, D., Wang, Y., 2018. Apatite stability under different oxygen fugacities relevant to planetary bodies. Mineral. Petrol. 112 (6), 789–800.
Trail, D., Bindeman, I.N., Watson, E.B., Schmitt, A.K., 2009. Experimental calibration of oxygen isotope fractionation between quartz and zircon. Geochim. Cosmochim. Acta 73, 7110–7126.
Trail, D., Watson, E.B., Tailby, N.D., 2011a. The oxidation state of Hadean magmas and implications for early Earth's atmosphere. Nature 480, 79–82.
Trail, D., Thomas, J.B., Watson, E.B., 2011b. The incorporation of hydroxyl into zircon. Am. Mineral. 96, 60–67.
Trail, D., Watson, E.B., Tailby, N.D., 2012. Ce and Eu anomalies in zircon as proxies for the oxidation state of magmas. Geochim. Cosmochim. Acta 97, 70–87.

Trail, D., Tailby, N.D., Lanzirotti, A., Newville, M., Thomas, J.B., Watson, E.B., 2015. Magma redox evolution of silicic magmas: insights from high spatial resolution Ce^{4+}/Ce^{3+} measurements of single Bishop Tuff zircons. Chem. Geol. 402, 77–88.

Trail, D., Boehnke, P., Savage, P.S., Liu, M.C., Miller, M.L., Bindeman, I., 2018. Origin and significance of Si and O isotope heterogeneities in Phanerozoic, Archean, and Hadean zircon. Proc. Natl. Acad. Sci. USA 115, 10287–10292.

Trail, D., McCollom, T.M., 2023. Relatively oxidized fluids fed Earth's earliest hydrothermal systems. Science 379, 582–585.

Trail, D., Mojzsis, S.J., Harrison, T.M., Schmitt, A.K., Watson, E.B., Young, E.D., 2007. Constraints on Hadean zircon protoliths from oxygen isotopes, Ti-thermometry, and rare earth elements. Geochem. Geophys. Geosyst. 8 (6) https://doi.org/10.1029/2006gc001449.

Trail, D., Savage, P.S., Moynier, F., 2019. Experimentally determined Si isotope fractionation between zircon and quartz. Geochim. Cosmochim. Acta 260, 257–274.

Walsh, J.M.J., Spandler, C., 2023. The role of zircon in hydrothermal heavy REE mineralisation: the case for unconformity-related ore deposits of north-west Australia. Chem. Geol. 629.

Watson, E.B., Green, T.H., 1981. Apatite/liquid partition coefficients for the rare earth elements and strontium.Earth Planet. Sci. Lett. 56, 405–421.

Xia, Q.-X., Zheng, Y.-F., Zhou, L.G., 2008. Dehydration and melting during continental collision: constraints from element and isotope geochemistry of low-T/UHP granitic gneiss in the Dabie orogen. Chem. Geol. 247, 36–65.

Xia, Q.-X., Zheng, Y.-F., Hu, Z., 2010. Trace elements in zircon and coexisting minerals from low-T/UHP metagranite in the Dabie orogen: Implications for action of supercritical fluid during continental subduction-zone metamorphism. Lithos 114 (3–4), 385–412.

Yang, W.-B., Niu, H.-C., Shan, Q., Sun, W.-D., Zhang, H., Li, N.-B., Jiang, Y.-H., Yu, X.-Y., 2013. Geochemistry of magmatic and hydrothermal zircon from the highly evolved Baerzhe alkaline granite: implications for Zr–REE–Nb mineralization. Mineralium Deposita 49, 451–470.

Yardley, B.W.D., Bodnar, R.J., 2014. Fluids in the continental crust. Geochem. Perspect. 3, 1–127.

Yardley, B.W.D., Graham, J.T., 2002. The origins of salinity in metamorphic fluids. Geofluids 2, 249–256.

Yui, T.-F., Maki, K., Usuki, T., Lan, C.-Y., Martens, U., Wu, C.-M., Wu, T.-W., Liou, J.G., 2010. Genesis of Guatemala jadeitite and related fluid characteristics: Insight from zircon. Chem. Geol. 270 (1–4), 45–55.

Yui, T.-F., Maki, K., Wang, K.-L., Lan, C.-Y., Usuki, T., Iizuka, Y., Wu, C.-M., Wu, T.-W., Nishiyama, T., Martens, U., Liou, J.G., Grove, M., 2012. Hf isotope and REE compositions of zircon from jadeitite (Tone, Japan and north of the Motagua fault, Guatemala): implications on jadeitite genesis and possible protoliths. Eur. J. Mineral. 24 (2), 263–275.

Zhai, W., Zhang, E., Zheng, S.-Q., Santosh, M., Sun, X.-M., Niu, H.-C., Fu, B., Fu, Y., Li, D.-F., Jiang, Y.-H., Liang, F., Lin, W.-P., Zhao, Y., Han, S.-Y., 2022. Hydrothermal zircon: characteristics, genesis and metallogenic implications. Ore Geol. Rev. 149.